Dynamic Impedance Studies of Oxidation of Nickel and Glycerol at Nickel Electrodes.

by

Mohammad Alikarami
B.Sc., University of Tehran (2016)

A Thesis Submitted in Partial Fulfillment of the
Requirements for the Degree of

Master of Science

in the Department of Chemistry

Dynamic Impedance Studies of Oxidation of Nickel and Glycerol at Nickel Electrodes.

by

Mohammad Alikarami

B.Sc., University of Tehran (2016)

Supervisory Committee

Dr. D. A. Harrington, Supervisor (Department of Chemistry)

Dr. I. Paci, Departmental Member (Department of Chemistry)

Supervisory Committee

Dr. D. A. Harrington, Supervisor (Department of Chemistry)

Dr. I. Paci, Departmental Member (Department of Chemistry)

Abstract

This thesis uses dynamic electrochemical impedance spectroscopy (dEIS) to study how nickel undergoes electrooxidation. An electropolishing step is used to make a clean surface, and then the transformation of nickel to α-$Ni(OH)_2$ is studied, including how a holding potential affects the double layer capacitance, surface structure and charge transfer resistance. Also, NiOOH is grown on the surface by sweeping to more positive potentials, and the activity of NiOOH toward glycerol electrooxidation is studied. It is shown that the free water content decreases on the surface (all or some portions of the surface, or possibly one or two monolayers close to the nickel surface) during the potential hold as determined by the decrease in measured capacitance. Oxidation of glycerol to glyceraldehyde is found to be the main reaction and the reaction mechanism is discussed.

Table of Contents

List of Figures

Nomenclature

α	Charge transfer coefficient, 1
β	Symmetry factor, 1
θ	Surface coverage, 1
η	Overpotential, V
σ	Charge density, μC m^{-2}
ϕ	Phase lag, rad
ϕ_{i}	Potential of the component i, V
μ_{i}	Chemical potential of component i in the solution, J mol^{-1}
μ_{i}^{0}	Standard chemical potential of component i, J mol^{-1}
Γ_{i}	Surface concentration, mol m^{-2}
ν	Reaction rate, mol m^{-2} s^{-1}
χ^2	Chi-squared fit parameter, 1
ω	Angular frequency, rad s^{-1}
a_{i}	Activity of the component i in the solution, 1
AC	Alternating current
ADC	Analog to digital converter
b	Warburg impedance element, s$^{0.5}$
b	Tafel slope, mV/dec
C^*	Concentration of diffusing species, mol m^{-3}
c_{i}	Concentration of the ion i, mol m^{-3}
C	Capacitance, F cm^{-2}
C'	Real part of capacitance, F cm^{-2}
C"	Imaginary part of capacitance, F cm^{-2}
C_{dl}	Double layer capacitance, F cm^{-2}

C_{comL}	Compact layer capacitance, F cm^{-2}
C_{difL}	Diffuse layer capacitance, F cm^{-2}
C_{eff}	Effective capacitance, F cm^{-2}
CDF	Cumulative probability density function
CPE	Constant phase element
CV	Cyclic voltammogram
d	Thickness of diffusion layer in NiOOH region, m
D	Diffusion coefficient, m^2 s^{-1}
DAC	Digital to analog converter
DC	Direct current
dEIS	Dynamic electrochemical impedance spectroscopy
DHA	dihydroxyacetone
E	Potential, V
$\widetilde{E}(\omega)$	Fourier transformed potential
E^0	Standard electrode potential, V
ECSA	Electrochemical active surface area, m^2
EQCM	Electrochemical quartz crystal microbalance
F	Faraday's constant, C mol^{-1}
f	Frequency, Hz
G	Gibbs free energy, kJ mol^{-1}
HER	Hydrogen evolution reaction
HPLC	High-performance liquid chromatography
i	$\sqrt{-1}$
$\widetilde{I}(\omega)$	Fourier transformed current
j	Current density, A cm^{-2}
$\widetilde{j}(\omega)$	Fourier transformed current density
j_0	Exchange current density, A cm^{-2}
j_{p}	Peak current density, A cm^{-2}
J_{i}	Flux of the ion i, mol m^{-2} s^{-1}
k	Rate constant

K	Equilibrium constant
m	mass, g
n	Constant phase element parameter, 1
O	Finite Warburg element (short)
OER	Oxygen evolution reaction
PZC	Potential of the zero charge, V
Q	Constant phase element
R	Ideal gas constant, J mol^{-1} K^{-1}
R_{ct}	Charge transfer resistance, Ω cm^2
R_p	Polarization resistance, Ω cm^2
R_s	Solution resistance, Ω cm^2
RDS	Rate determining step
RHE	Reversible hydrogen electrode
STM	Scanning tunnelling microscopy
T	Temperature, K
t	Time, s
u_i	Mobility of the ion, m^2 V^{-1} s^{-1}
ν	sweep rate, V s^{-1}
XPS	X-ray photoelectron spectroscopy
Y	Admittance, S cm^{-2}
Y_0	Admittance of CPE, S s^n cm^{-2}
$\|Y\|$	Magnitude of admittance, S cm^{-2}
Y_{warb}	Finite Warburg parameter, mS cm^{-2}
Z	Impedance, Ω cm^2
Z'	Real part of impedance, Ω cm^2
Z''	Imaginary part of impedance, Ω cm^2
$\|Z\|$	Magnitude of impedance, Ω cm^2
z_i	Charge number of ion, 1
z	Number of electrons transferred

Acknowledgements

I would like to thank David Harrington who prompted me to continue my studies, all my group members at University of Victoria, Tianyu, Victor, Han, Tory and Natalie that I enjoyed spending time with, and all the staff members, secretaries and Senior Lab Instructors.

Special thanks to all the faculty members in the department and my committee members; my interactions and discussions with all of them have been very helpful.

To my beloved mother, father and sister.

Chapter 1

Introduction

1.1 Objective

Environmental issues like global warming are a real threat for humankind. A change in energy supply from fossil fuels to renewable sources like wind and solar is necessary. However, there are fluctuations in supply, e.g. some days are more sunny and more energy is available to extract, or at nights there is no available solar energy supply although there is demand for electricity. Therefore, a solution for storing electricity is required. One of the best ways to store electricity is to store it in the form of chemical energy. It consists of converting electricity to hydrogen and oxygen in an electrolyzer. In this way electricity can be regained in case of need by converting hydrogen and oxygen to water using fuel cell technology. Conventionally acid media electrolysers with proton exchange membrane and platinum (Pt) electrocatalysts have been used for water oxidation, but during the last years there has been a lot of research on alkaline electrolysers and nickel has showed a great performance comparable to the efficiencies in the acid media. Alkaline media has the advantage of decreasing the rate of corrosion, however the reaction mechanism is usually more complicated in the alkaline solutions.

Electrooxidation of liquid fuels like methanol, ethanol and glycerol usually consists of several reaction steps that can be either chemical or electrochemical steps. The mechanism of reaction is different for different electrocatalysts. Understanding the mechanism behind each of these steps for nickel electrodes can enable us to have better Ni-based catalyst design, with higher activity and selectivity toward desired products. Concentration of the fuel and electrolyte, temperature, catalyst shape, pH, etc. are other factors that should be considered for optimum catalyst design.

In this thesis, electrochemical methods are used to unravel the mechanism of formation of different oxide phases of nickel and also the mechanism for glycerol oxidation. Dynamic electrochemical impedance spectroscopy (dEIS) is the primary technique used in this thesis, that enables us to study the different time constants in the reaction mechansim using AC voltammetry. Some of the background topics and techniques used in this thesis are now briefly described.

1.2 Definitions and Experimental Methods

1.2.1 Electrochemical Reaction

Assume the following one electron transfer reaction.

$$A(aq)+e^- \leftrightarrows A^-(aq) \tag{1.1}$$

The reaction can be explained by electron transfer between electronic states of electrode and A and A^- species. A comes up to the electrode, receives the electron from the electrode to become A^-, which then moves away.

At equilibrium, the overall rate of electron transfer is zero. When more negative potential than equilibrium potential is applied to the system, the electrode Fermi level moves to higher values and enables electron transfer from the electrode to empty

energy levels of A species and the reduction reaction (1.1) occurs. The opposite happens at more positive potentials than the equilibrium potential; the Fermi level comes down and promotes oxidation, the reverse reaction in (1.1).

The tendency of species to move or react is determined by their electrochemical potential ($\widetilde{\mu}_{\mathrm{i}}$), Based on the Eq. 1.2. Where z_{i} is the charge number of the ion, F is Faraday's constant, T is temperature, R is the ideal gas constant, a_{i} is the activity, ϕ_{i} is the potential and μ_{i}^{0} is the standard chemical potential.

$$\widetilde{\mu}_{\mathrm{i}} = \mu_{\mathrm{i}}^{0} + RT \ln (a_{\mathrm{i}}) + z_{\mathrm{i}} F \phi_{\mathrm{i}} \tag{1.2}$$

$$\mu_{\mathrm{i}} = \mu_{\mathrm{i}}^{0} + RT \ln (a_{\mathrm{i}}) \tag{1.3}$$

Eq. 1.3 shows that chemical potential changes, by changing the activity of the ions in the solution.

Interface

At the interface the driving force for the reaction (1.1) can be written as the difference between electrohemical potential of products and reactants (Eq. 1.4).

$$\widetilde{\Delta G} = \widetilde{\mu}_{\mathrm{A^-}} - \widetilde{\mu}_{\mathrm{e^-}} - \widetilde{\mu}_{\mathrm{A}} \tag{1.4}$$

Combining Eq. (1.2) and Eq. 1.4, results in:

$$\widetilde{\Delta G} = (\mu_{\mathrm{A^-}} - F\phi_{\mathrm{s}}) - (\mu_{\mathrm{e^-}} - F\phi_{\mathrm{m}}) - (\mu_{\mathrm{A}}) \tag{1.5}$$

$$\widetilde{\Delta G} = \mu_{\mathrm{A^-}} - \mu_{\mathrm{e^-}} - \mu_{\mathrm{A}} + F\,(\phi_{\mathrm{m}} - \phi_{\mathrm{s}}) \tag{1.6}$$

Where, μ_{i} is the chemical potential, ϕ_{m} is the potential on the metal (electrode) and ϕ_{s} is the potential in the solution side of the double layer.

And, the electrode potential is related to the potential drop at the interface by,

$$E = (\phi_{\mathrm{m}} - \phi_{\mathrm{s}}) + \text{const} \tag{1.7}$$

Where the constant depends on the reference electrode.

Oxidation consists of transfer of electrons from electrolyte (for example: $Ni + 2OH^- \rightarrow Ni(OH)_2 + 2e^-$) into the electrode. When electrode has more positive potential, it acts like a stronger magnet that attracts more electrons, and these electrons are provided by the oxidation reaction. The rate of the oxidation reaction is increased to provide the more electrons that are needed.

Solution (diffusion layer)

In the solution, a species moves if there is a gradient in its electrochemical potential (which can be due a gradient either in the activity of the species or to the potentials) according to the Eq. (1.8)

$$\frac{\partial \widetilde{\mu_{\mathrm{i}}}}{\partial x} = \frac{\partial \mu_{\mathrm{i}}}{\partial x} + z_{\mathrm{i}} F \frac{\partial \phi}{\partial x} \tag{1.8}$$

The first term in Eq. (1.8) leads to diffusion and the second term leads to migration, and after approximation and suitable manipulation, leads to the Nernst-Planck equation. In Eq. 1.9 J_{i} is the flux of the ion, D is the diffusion coefficient, and u_{i} is the mobility of the component i in the fluid. It shows that movement of ions is due to the concentration gradient and potential gradient. The movement because of the concentration gradient is called, diffusion and the movement because of the potential gradient is called, migration.

$$J_{\mathrm{i}} = -D\,\frac{\partial c_{\mathrm{i}}}{\partial x} + z_{\mathrm{i}} F u_{\mathrm{i}} c_{\mathrm{i}} \frac{\partial \phi}{\partial x} \tag{1.9}$$

1.2.2 Double layer

Electrochemical reactions take place at the interface between electrode and solution, and so it is usually the most important region affecting the reaction mechanism. In the case of solutions with high concentrations of ions, the potential drop occurs only at the interface, which is called the double layer. The thickness of this layer is around 3 to 10 Å.

The potential drop at the interface occurs in two regions: 1) a compact layer that consists of inner Helmholtz layer and outer Helmholtz layer, which mostly consists of solvent molecules that are usually polarized in the strong field near the electrode, and adsorbed ions that can be adsorbed on to the electrode, and 2) diffuse layer. Inner Helmholtz layer is the thinnest layer close to the electrode that consist only one layer of solvent molecules that are polarized near the electrode, and the main part of the potential drop occurs in this layer. In outer Helmholtz layer electric field is still strong, and ions are mostly solvated by the water. Diffuse layer is where electric field is weaker, but still affects the ions. Ideally all the potential drop should be just in compact layer because this is the potential that is felt by species close to the electrode that will undergo electron transfer reactions. The equivalent circuit for the double layer consists of a series combination of the compact layer capacitance and the diffuse layer capacitance, so the total capacitance equals:

$$\frac{1}{C_{\mathrm{dl}}} = \frac{1}{C_{\mathrm{comL}}} + \frac{1}{C_{\mathrm{difL}}} \tag{1.10}$$

Electron transfer is not essentially involved in double layer charging; even approaching ions can change the electric field in the double layer region and lead to

induced current flow.

1.3 Electrochemical Methods

Cyclic voltammetry, sweep hold sweep and dEIS are the main methods used here to study different phases of nickel and glycerol oxidation.

1.3.1 Cyclic voltammetry (CV)

CV is the most common technique in electrochemistry. In this technique, the potential is swept from a starting point, E_{s}, to an upper limit, E_{up}, then back from the upper limit to the lower limit, E_{low}. CV is a quick method to find potentials at which each electrochemical reaction occurs. Doing this experiment at different sweep rates enables us to find more information about reversibility, charge dependency on sweep rate and even, by simulating CV, obtaining some kinetic parameters.

1.3.2 Sweep hold sweep

In sweep hold sweep experiments, first CV is done until the desired potential, then potential is held at this potential until some desired time, then again potential is swept in the desired direction. In this thesis, this method is used to grow the oxide layer in hydroxide region and then observe the change in the reduction charge.

1.3.3 Impedance Spectroscopy

In impedance spectroscopy, the response to a small sinusoidal perturbation in current or potential is measured. To do the potentiostatic impedance, the DC potential is set at a desired value, and after waiting until steady state current is observed, a

perturbation at different frequencies is applied to the system and AC current responses are measured.

If the following sine wave potential (Eq. 1.11) is applied to the system, the current response is a sine wave with a phase lag (1.12).

$$E = E_{\mathrm{dc}} + |E| \sin \omega t \tag{1.11}$$

$$I = I_{\mathrm{dc}} + |I\ | \sin (\omega t + \phi) \tag{1.12}$$

Transforming the current to the frequency domain to separate the output current into its frequency dependent components results in:

$$\widetilde{I}(\omega) = |I\ | \cos \phi + \mathrm{i}|I\ | \sin \phi \tag{1.13}$$

Similarly, the potential gives,

$$\widetilde{E}(\omega) = |E| \tag{1.14}$$

Then the impedance can be calculated by the ratio of transformed potential over transformed current from Eq. 1.15.

$$\mathrm{Z}(\omega) = \frac{\widetilde{E}(\omega)}{\widetilde{j}(\omega)} \tag{1.15}$$

The impedance response, both real and imaginary parts, carries information about the reaction mechanism and the time constants for different processes going on. Two different approaches can be used for analysis of the data. Deriving a mathematical model and finding the impedance response and comparing the simulated results with

experimental results is one approach. The other approach is using equivalent circuits. In this approach a circuit that closely fit with experimental results is suggested, and values of different elements of the circuit are related to processes in the system (double layer charging, charge transfer, adsorption, etc.).

Impedance experiments can be performed either by applying a single frequency sine wave and repeating the experiment at different frequencies, or simultaneously applying different frequencies and performing a fast Fourier transform.

In the multisine approach, the AC potential in all the frequencies are applied at the same time so, the measurement is much faster and limited by the lowest frequency applied to the cell. More consistent data are acquired by multisine signal because the measurement for all the frequencies are done simultaneously [1].

However, intermodulation frequencies are present with multisines at the sum and difference of the applied frequencies, usually the frequencies that are applied to cell are chosen in a way that minimizes the contribution from harmonic generation. The rule is choosing a frequency which is not the main harmonic generation frequency of lower frequencies or sum and difference frequencies. This can be achieved to a good approximation by choosing all odd multipliers). The other frequencies were chosen as multipliers of the base frequency, using the Popkirov criteria [2]. For choosing the amplitude, a "2:10" rule was used in which high frequency signals had lower amplitude, decreasing the amplitude by one half for every decade increase in the frequency [3].

1.3.4 Dynamic Electrochemical Impedance Spectroscopy

In dynamic impedance spectroscopy unlike conventional potentiostatic impedance, the AC potential is applied simultaneously with CV. It allows studying non steady state processes that are inaccessible with potentiostatic impedance. The Direct current (DC) ramp potential (like a CV, where DC potential is swept from some initial

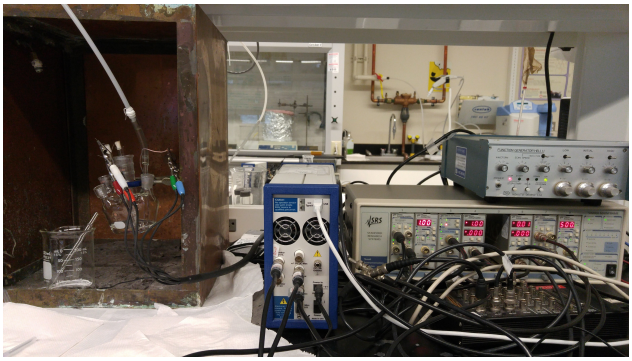

Figure 1.1: Setup for dEIS experiment

value to a final value) is added to the AC multisine potential. Then the AC+DC potential is applied to the electrochemical cell. The output current and potentials are digitized and then the real and imaginary parts of the impedance are calculated by a fast Fourier transform.

The minimum frequency is limited by the sweep rate and how fast surface conditions change. In our study for 5 mV s^{-1}, 1 Hz was chosen as the lowest (base) frequency. Criteria for choosing the low frequency can be based on equation below [4]. This equation demonstrates that the minimum frequency that we can use increases by increasing sweep rate. By increasing sweep rate, the DC potential changes a lot during an AC cycle, which makes measurement unreliable, because the assumption is that during an AC cycle, DC potential is almost constant.

$$\frac{F\nu}{RT} \ll \omega_{\min} \tag{1.16}$$

Fig. 1.1 shows the setup for dEIS including a function generator, potentiostat and ADC/DAC converter. Function generator is used for applying potential, choosing sweep rate, choosing potential range for the sweep, and also holding and sweeping the potential.

1.4 Data Fitting and Equivalent Circuits

Fitting the experimental data (real and imaginary parts of impedance) with a circuit model helps to get more insight about the processes going on at each specific potential. In the process of fitting, parameters of models are changed to minimize χ^2, that is the indicator of how good is the fit. χ^2 demonstrates the errors assciated with the difference between the model and experimental data. Usually adding more parameters to the model decreases the χ^2, however change in χ^2 should be big enough. F test is a tool usually used to find out whether this change is significant or not.

1.4.1 F Test

To choose between possible equivalent circuit model F test, Eq. 1.17, was done to make sure if adding a new element to the equivalent circuit is statically reasonable.

$$F_{\chi^2}=\frac{\chi^2_{\text{old}}\text{-}\chi^2_{\text{new}}}{\chi^2_{\text{new}}}\left(\frac{\upsilon_{\text{new}}}{\beta}\right) \tag{1.17}$$

ν is degree of freedom, ν=2 (no of frequencies) - (no of elements parameters in the new circuit) , and β is the number of parameters added in new model that equals to 1 (even if we replace capacitor with CPE, number of new parameters is 1).

χ^2 is the fit quality parameter and demonstrates the standard deviation of the fitted circuit and the experimental data, so it is a measure of the quality of the fitting. The lower χ^2 value, shows a better fit. Adding a new parameter usually decreases the χ^2, but in order to see if this decrease is significant, F-test can be used.

1.5 Nickel Voltammetry

In this section, the voltammetry of nickel to its oxidation products in introduced. Fig. 1.2 shows that the electrooxidation of nickel to α-$Ni(OH)_2$ occurs at around 0.2 V

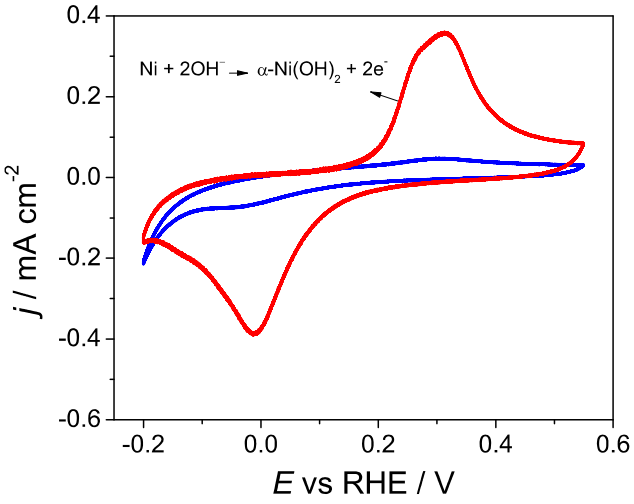

Figure 1.2: Voltammogram of nickel with and without electropolished nickel at 100 mV s^{-1} and in 0.5 M KOH. Red: electropolished, blue: unelectropolished.

and it continues growing by going to more positive potentials (0.5 V to 1.3 V). Aging and more positive potentials promotes formation of β-$Ni(OH)_2$ from α-$Ni(OH)_2$ (see chapter 2 for more details). The corresponding reduction of this oxide layer has peak minimum at around 0 V.

As can be seen without electropolishing the oxidation and reduction peaks are not pronounced, which demonstrates corrosion resistance of the unelectropolished electrode because of the presence of the passivating oxide layer. This passivating layer can be removed by electropolishing (holding the current at 1.8 A cm^{-2} for 10 s, in phosphoric acid solution, see chapter 2 for more details).

The charge under the α-$Ni(OH)_2$ peak is proportional to the active surface area of the electrode.Assuming two electrons per nickel atom, 514 μC cm^{-2} was used for area normalization. This is the charge required for formation of one monolayer of nickel hydroxide.

Fig. 1.3 shows the third cycle after electropolishing in the potential range where the $Ni(OH)_2$ to NiOOH transformation occurs. $Ni(OH)_2$ at the onset potential (1.35

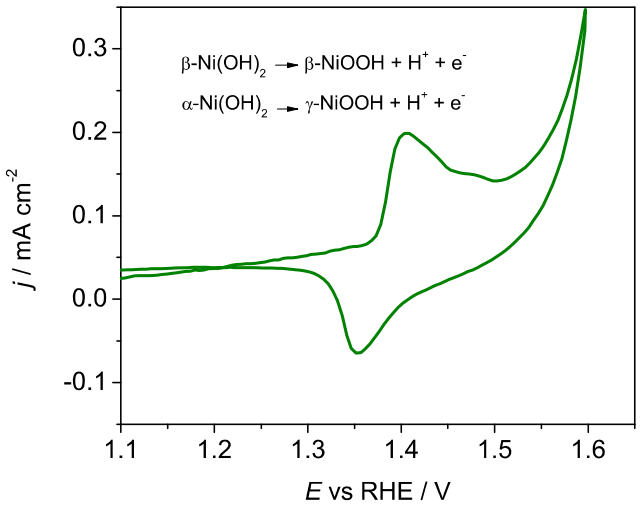

Figure 1.3: NiOOH oxidation and reduction peaks after electropolishing. 5 mV s^{-1}, 3rd cycle in 0.5 M KOH.

V) is possibly the mixture of α-$Ni(OH)_2$ and β-$Ni(OH)_2$ phase, because the α-$Ni(OH)_2$ to β-$Ni(OH)_2$ conversion occurs in the potental range of 0.5 V to 1.3 V. The amount of α-$Ni(OH)_2$ and β-$Ni(OH)_2$ before this peak is a function of seep rate, and the rate of interconversion of α-$Ni(OH)_2$ to β-$Ni(OH)_2$. The reduction peak potential is at around 1.35 V.

1.6 Nickel Structure and Application Review

This section introduces the common phases of oxidation products of nickel. $Ni(OH)_2$ has two phases, more crystalline β-$Ni(OH)_2$ and less crystalline α-$Ni(OH)_2$.

β-$Ni(OH)_2$ is a p-type semiconductor with a band gap of around 4 eV [5]. It has a brucite-like structure like $Mg(OH)_2$ in the P3m1 space group with trigonal crystal symmetry and hexagonal lattice [6]. The parameters for the hexagonal unit cell are: $a = 3.126$ Å, $c = 4.605$ Å [7]. The α phase has not been well characterized because of its lower cystallinity. The interlayer spacing is believed to be the most prominent

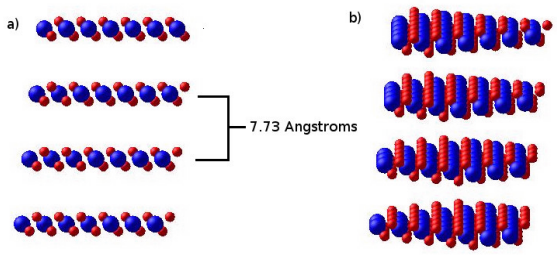

Figure 1.4: α-Ni(OH)$_2$ structure. Blue: nickel, red: oxygen. a) and b) are different views.

difference between these two phases. α-Ni(OH)$_2$ has higher interplanar spacing than ordered β-Ni(OH)$_2$: 7.6 Å and 4.6 Å for the α and β phases, respectively. The presence of water or ions in the interlayer in α phase is the reason for this difference.

No hydrogen bonding was observed in the crystal structure of β-Ni(OH)$_2$ between OH groups of each layer, however for the α phase there is hydrogen bonding between intercalated water and OH groups of the nickel hydroxide layers [7]. Bantignies et al. also studied Ni(OH)$_2$ and proposed that interlayer interactions are electrostatic in nature and no hydrogen bonding is present [8]. Fig. 1.4 shows the layered structure of α-Ni(OH)$_2$ (the only difference between α and β phase is the interlayer spacing, so only one of them is shown here).

β-NiOOH is in the C2/m space group. Tkalych et al. proposed, based on density functional theory calculations, that β-NiOOH has a structure with a staggered arrangement of protons (protons are present on both sides of each layer) and that the Jahn-Teller distortion of the low spin octahedral Ni^{3+} center might be the explanation for two different Ni-O bond distances experimentally observed for this phase [5, 9]. EXAFS studies of β-NiOOH have shown Ni-O distances of 1.88 and 2.07 Å, and Ni-Ni distances of 2.82 and 3.13 Å. Possibly nickel ions (Ni^{3+}) are in distorted octahedral form with Jahn-Teller distortion, rather than a mixture of Ni^{2+} and Ni^{4+} [5].

Hydrogen bonding between the layers is observed for phases except β-Ni(OH)$_2$ [7].

γ-NiOOH has a rhombohedral unit cell with some distortions and a higher oxida-

tion state compared to the β phase, implying the presence of sodium or potassium ions that balance the excess charge on nickel.

1.7 Initial Stages of $Ni(OH)_2$ Formation

During the last decade a lot of effort on replacement of noble-metal oxygen evolution reaction (OER) catalysts with earth abundant metals like Ni and Fe have been made [10–13]. Nickel has also been used for lactic acid oxidation [14], glucose oxidation [15], glycerol electrooxidation [16, 17], and the oxygen reduction reaction (ORR) [18, 19].

In basic solution the nickel surface is covered with a oxide layer. The nature of the species that form on oxidizing Ni electrode in alkaline solution has been studied for a long time [20–22]. Bode summarized the formation and interconversion of the various hydroxide and oxyhydroxide phases in terms of time and potential [20]. The initially formed oxide is believed to be a hydrated hydroxide, α-$Ni(OH)_2$, which is formed at around 0.2 V vs RHE and, irreversibly interconverts to a less hydrated β-$Ni(OH)_2$ at higher than 0.5 V.

There are still doubts on the mechanism and nature of species on early stages of nickel oxidation. Seyeux using in situ scanning tunnelling microscopy (STM) in 1 mM NaOH observed dissolution of step defects and nucleation of initial oxides on these step defects in the potential region before nickel oxidation (lower than 0.2 V vs RHE) however they didn't conclude dissolution-reprecipitation. They observed slow growth in this potential region and nucleation and dissolution was the main process observed. They found a hexagonal lattice parameter using STM that was closer to β-$Ni(OH)_2$ in the potential region of nickel oxide formation in early stages of oxidation [23], However Macdougall et al added $NiSO_4$ to the solution (0.15 M Na_2SO_4 at pH 8.4) and did not observe any change in galvanostatic charging curve, and concluded the oxide did not form by a dissolution reprecipitation mechanism [21]. The amount of dissolution

is pH dependent and less dissolution is expected in the more alkaline solutions.

Klaus et al. found evidence for the α to β aging process by quartz crystal microbalance (QCM) experiments [14]. The aging was done by keeping the nickel electrodes in KOH solution without applying any potential. Hahn used IR reflectance to study this transformation (the α to β) by looking at the spectra at different steady potentials, they attributed the band at 3650 cm^{-1} to OH vibration in α-$Ni(OH)_2$ (around 0.3 V). At 0.45 V they observed an additional weak band at 3200 cm^{-1} due to the OH bond of water inserted in the nickel hydroxide layer. Around 0.6 V they observed the α to β transformation: the observed shift of the OH band from 3650 to 3450 cm^{-1} was related to strengthening NiO bonds and weakening OH bonds [22]. This shift might also be due to hydrogen bonding of intercalated water to OH groups in $Ni(OH)_2$. O'Brien [24] carried out reduction at 10 mA cm^{-2} after holding at different potentials, and observed longer times to reach steady-state hydrogen evolution reaction (HER) currents for hold potentials up to about 0.2 V, around the onset potential for nickel oxidation. Holding at higher than 0.2 V led to a decrease in reduction time. They attributed this increase in charge mostly to nickel oxide reduction and not HER, becoming steady between 0.2 and 0.3 V and then the decrease in charge was explained by conversion of α-$Ni(OH)_2$ to β-$Ni(OH)_2$. Huq observed higher activity for HER in alkaline media compared to acidic media [25].

Most of the literature on nickel hydroxide formation for the early stages and considers the oxides formed potentiostatically at potentials higher than 0.5 V have more than a few monolayers of oxide. Results of the ones higher than 0.5 V, show that nickel oxide consists of an inner NiO layer, and an outer $Ni(OH)_2$ layer that is most probably hydrated; thickness of both these layers increases by going to more positive potentials, until the onset potential for NiOOH. Total thickness of the oxide layer ranges from 9 to 12 Å (mostly NiO in acidic solution). Larger thicknesses were observed for alkaline compared to acidic solutions [26–29], total thicknesses of 10 Å and 20 Å were observed after 30 minutes polarization at around 0.5 V and 1.3 V,

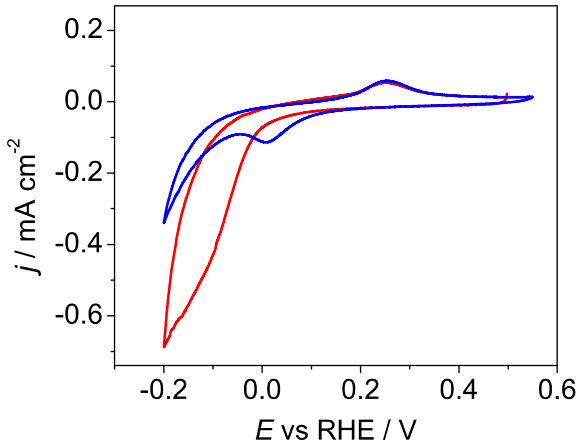

Figure 1.5: First (Red) and second (blue) cycle at sweep rate of 20 mV s^{-1}, after holding the potential for 1 hour at 0.5 V.

respectively, corresponding to only a few monolayers growth at 0.5 V. [30].

Fig. 1.5 shows the potential regions for oxidation of nickel to α-$Ni(OH)_2$ and its reduction. Oxidation starts at around 0.2 V, and α-$Ni(OH)_2$ continues to grow after this potential with simultaneous conversion to β-$Ni(OH)_2$, in the reduction region it can be seen that after holding the potential at 0.5 V, the grown oxide layer can be reduced almost completely due to observing same anodic charge in first and second cycle after holding.

The reduction peak for nickel hydroxide is more pronounced at lower sweep rates. After holding at potentials more positive than 0.7 V, at high sweep rates, no reduction peak can be observed. Also, holding the potential at more positive than around 0.9 V decreases the oxidation charge in the second forward going cycle, at the sweep rate of 5 mV s^{-1}.

Having a oxide free surface is a necessity for studying early stages of oxidation, so a preparation procedure is needed to remove the native oxide. Seyeux using STM observed an oxide-free surface in the potential region before nickel oxidation for their electropolished and hydrogen annealed electrode [23]. At pH 8.4, Macdougall observed

no change in X-ray diffraction pattern of passivated films after holding at around -0.25 V, and concluded that oxide layers with thicknesses in the range of 9 to 12 Å can't be reduced, while oxide layers produced by air exposure of an electropolished electrode, with thicknesses 6 - 8 Å could be reduced. Both these layers were assigned to be NiO, with the oxide on the electropolished electrode showing a 2% expansion [21].

Okazawa et al. studied oxide growth on Nickel(1 1 1) by isotopically labelled high-resolution medium energy ion scattering [31] and observed diffusion of nickel atoms to the surface from the bulk. They learned that it is the nickel atoms that diffuse not oxygen.

Hu observed isopotential points in the forward and backward sweeps when changing the upper limit of voltammograms, and attributed this to the presence of two reactions that compete for the same sites on the nickel surface, namely hydrogen desorption and nickel hydroxide formation [32]. They also observed a decrease in the ratio of the peak current in the first cycle to the peak current in the fifth cycle, this ratio became zero at around 1.25 V (in the potential range of α-$Ni(OH)_2$ and β-$Ni(OH)_2$). For nickel on glassy carbon, the current was reduced to 30% after five cycles at this potential and stayed almost the same going to more positive potentials.

Dynamic electrochemical impedance spectroscopy (dEIS) is a strong tool for studying reaction mechanisms and deducing reaction steps and intermediates. There are only a few studies of the initial stages of Ni oxidation using EIS [33–37]. Here we leverage the advantages of dEIS in comparison to potentiostatic EIS for studying systems that have fast kinetics and change with time, such as the conversion of α-$Ni(OH)_2$ and β-$Ni(OH)_2$. This method enables us to study unsteady-state conditions such as the change in coverage of species during cyclic voltammograms. This method has been previously used for methanol oxidation on Pt [38]. dEIS has been used for studying nickel hydroxide formation before [35], but the frequency range used was not suitable to see the slow processes occurring. In their proposed mechanism they suggested initial OH^- adsorption before formation of α-$Ni(OH)_2$. Katic et al. applied

the point defect model and Mott–Schottky analysis to study oxidation of nickel electrodes polarized at 0.6 V for several hours. Their spectra showed features related to diffusion (Warburg elements) attributed to diffusion of point defects [36, 37]. Reid studied nickel oxidation using impedance spectroscopy and also observed Warburg elements [34]. However, the point defect model and Mott-Schottky analysis are derived for thicker films and do not seem to be suitable for the first few monolayers of oxidation.

In this work, we use dEIS and voltammetry to study the early stages of oxidation of a clean nickel surface and the aging and other structural changes that take place. Based on the experimental data, a reaction mechanism for the oxidation is proposed.

There are only a few studies in the lower than 0.5 V potential region that are relevant to this work. Hoppe et al. used XPS to study nickel hydroxide formation by potentiostatic holding for 300 s, at different potentials [26, 39]. They observed potential dependency of the phase and structure. However, identifying the phases in XPS for films of only one or two layers is difficult, and also doing XPS requires transfering the sample to vacuum that can dehydrate the sample.

1.8 $Ni(OH)_2$ to NiOOH transformation

Barnard et al. [40] discussed existence of activated and non activated α-$Ni(OH)_2$ to γ-NiOOH transformation. Activated and non activated transformation occurs before and after β-$Ni(OH)_2$ to β-NiOOH transformation, respectively.

Thermodynamically the α-$Ni(OH)_2$ to γ-NiOOH transformation should occur at less positive potentials compared to β-$Ni(OH)_2$ to β-NiOOH (more positive than 1.3 V) [41]. Also, due to overcharging the transformation of β-NiOOH to γ-NiOOH, it is difficult to assign specific potential ranges for each of the phases [6,42] (Check Fig.2.1 b) in Chap 2 for more details).

Takasaki [43] doing XRD observed full conversion of β-Ni(OH)$_2$ after charging (no signal for β-Ni(OH)$_2$ was observed), while just decrease in amount of α-Ni(OH)$_2$ by charging, also conversion of β-NiOOH to γ-NiOOH by charging at higher potentials. Also, K_xNiO_2 was detected at higher potentials. K_xNiO_2 was used to account for the charge of the nickel.

MacArthur et al. [44, 45] observed different features in the NiOOH oxidation peak (p_{a2}) (see chapter. 2). They attributed the first feature at lower potential (around 1.35 in RHE scale) to the reaction of α-Ni(OH)$_2$, and the second feature at slightly higher potential to the reaction of β-Ni(OH)$_2$. The first feature was higher in first cycle and decreased by cycling, the second feature increased by cycling.

Smith and coworkers studied Ni(OH)$_2$/NiOOH transformation and observed higher oxidation charge in the first cycle comparing to the second cycle. They proposed that more electrons are involved in the first oxidation cycle [46].

Corrigan used iodometry and spectroscopic measurements, and proposed the presence of only one mixed tetravalent and quadravalent phase in the NiOOH potential region, with average valence of 3.6. They also observed incomplete discharge, which they postulated formation of non conductive Ni(OH)$_2$, that makes a high resistant area (high potential drop) between nickel substrate and NiOOH layer, to be the reason [47].

1.9 Glycerol oxidation

Glycerol is a by-product of biodiesel production from biomass, and has a lot of potential for investment because of its availability and low price [48–50]. There are two possible electrochemical applications for glycerol. First, glycerol can be used for energy production due to its high energy density. Complete oxidation of glycerol to CO_2 can produce a lot of energy. Second, glycerol can be selectively electrooxidized

to more valuable products like dihydroxyacetone (DHA), glyceraldehyde, and glyceric acid. This work uses dEIS to address the mechanism for the production of these valuable oxidation products.

Considering both surface and glycerol, the following reactions can be proposed to explain the catalysis. Glycerol adsorption according to reaction (1.18) which is followed by another coupled electron-proton transfer (1.21), are probable reactions. The other Alternative is adsorption of glycerol on NiOOH surface according to the reaction (1.19) and then oxidation to glyceraldehyde with simultaneous reduction of NiOOH (1.20). Another possible pathway is direct oxidation of glycerol to glyceraldehyde according to (1.23) and (1.24). In this process, NiOOH that has already grown on the surface reduces to $Ni(OH)_2$ and provides the electrons needed for oxidation of glycerol to glyceraldehyde.

$$NiOOH + RCH_2OH \rightarrow Ni(OH)_2 + RCH_2O\ (ads) \tag{1.18}$$

$$RCH_2OH \rightarrow\ RCH_2O\ (ads) + H^+ + e^- \tag{1.19}$$

$$RCH_2O\ (ads) + NiOOH\ \rightarrow Ni(OH)_2 + RCHO \tag{1.20}$$

$$RCH_2O\ (ads) \rightarrow RCHO + H^+ + e^- \tag{1.21}$$

$$NiOOH + RCH_2OH \rightarrow Ni(OH)_2 + \text{product} \tag{1.22}$$

$$NiOOH + RCH_2OH \rightarrow Ni(OH)_2 + RCHO + H^+ + e^- \tag{1.23}$$

$$2\ NiOOH + RCH_2OH \rightarrow 2\ Ni(OH)_2 + RCHO \tag{1.24}$$

$$Ni(OH)_2 \rightleftharpoons NiOOH + H^+ + e^- \tag{1.25}$$

Where: R = -CH(OH)CH_2OH

Because the reaction is initiated only past the potential where NiOOH is formed, the active phase in the catalytic cycle for the glycerol oxidation is NiOOH, which is regenerated in the reaction (1.25). Reactions (1.22)-(1.24) are alternatives, where the difference is whether the electron transfer occurs and what is the product. Reactions (1.18) and (1.24) are the most probable reactions, because reaction (1.22) produces a product that is oxidised by one electron and there is not such a product observed in HPLC or proposed elsewhere. In the reaction (1.23), it is unlikely that simultaneous reduction of NiOOH and oxidation of glycerol produces an extra proton. If we assume reactions (1.24) and (1.25) in the catalytic cycle, also, assuming no adsorbed glycerol, and reaction on the surface, the rate of the reactions can be written as:

$$\nu_{1.24} = k_{1.24}\,\theta^2_{\mathrm{NiOOH}}\,c_{\mathrm{RCH_2OH}} \tag{1.26}$$

$$K_{1.25} = \frac{\theta_{\mathrm{NiOOH}}\,c_{\mathrm{H^+}}}{\theta_{\mathrm{Ni(OH)_2}}}\exp\left(\frac{F}{RT}\eta\right) \tag{1.27}$$

$$\Gamma_{\mathrm{m}}\frac{\mathrm{d}\theta_{\mathrm{NiOOH}}}{\mathrm{d}t} = -2\nu_{1.24} + \nu_{1.25} = 0 \tag{1.28}$$

$$\frac{j}{F} = \nu_{1.25} = 2\nu_{1.24} \tag{1.29}$$

$$1 = \theta_{\mathrm{NiOOH}} + \theta_{\mathrm{Ni(OH)_2}} \tag{1.30}$$

Also, θ_{NiOOH} should be small, because the surface coverages of RCH_2OH and RCHO are assumed to be negligible so the reaction (1.24) is fast, and as a result $\theta_{\mathrm{Ni(OH)_2}} \approx 1$

Some of the glycerol oxidation products are not stable in alkaline solution. Fig.

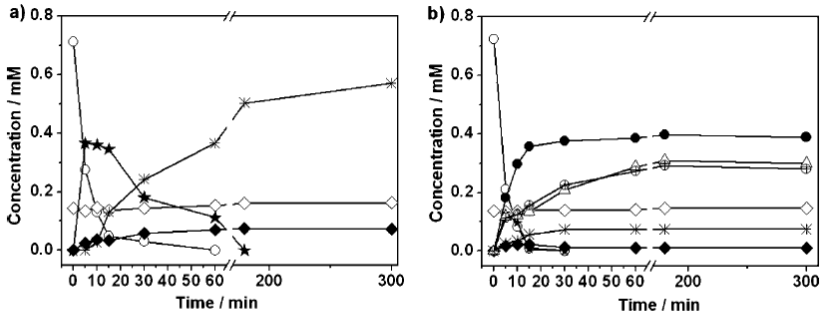

Figure 1. Glyceraldehyde degradation in 0.1 M NaOH as a function of reaction time under a) argon-saturated and b) non-deaerated conditions. ○: Glyceraldehyde; ★dihydroxyacetone; ●: glyceric acid; △: glycolic acid; ⊕: formic acid; ◇: dimer; ◆: fructose; ✳: lactic acid.

Figure 1.6: Glyceraldehyde decomposition in alkaline solution. Reprinted from [51], with permission. Copyright 2011 John Wiley and Sons.

1.6 shows the degradation of glyceraldehyde in 0.1 M NaOH without applying any potential in aerated and non-aerated conditions [51]. As can be seen, the decomposition is fast (faster in aerated solution), and these non-faradaic reactions make the electrochemical study of glycerol oxidation complicated. Koper's group [51] studied selectivity as a function of potential using HPLC on Pt and Au. Their proposed mechanism for oxidation consists of initial oxidation to glyceraldehyde that then oxidizes to glyceric acid, and further oxidation leads to production of glycolic acid and formic acid.

Nickel based catalysts have been widely used for alcohol oxidation [52]. HPLC and FTIR have been used to study product distribution and surface adsorbed species [17], Oliveira et al. observed mass transfer related processes by studying the glycerol oxidation anodic peak potential as a function of sweep rate, temperature and base and glycerol concentration on Ni/C electrodes [53]. They observed a linear relationship between anodic peak current and NaOH concentration. FTIR data showed the presence of only formate at higher glycerol concentrations (0.1 M); other compounds like carbonate and glycolate were observed at lower concentrations.

Kwon et al. [54] studied the effect of pK_a of the oxidation products on onset oxi-

dation potential and concluded that non faradaic reactions are the reason for having lower onset potential in lower pK_{a}. It can be reasoned by OH^- in the solution that promotes the chemical reactions. These chemical reactions have higher rates compared to the turnover rates of the hydroxides which are bound to the electrocatalyst.

Chapter 2

A Dynamic Impedance Study of the Initial Stages of Nickel Oxidation

This chapter was written as a self-contained journal paper, intended for later submission.

Initial stages of nickel oxidation is studied by dynamic electrochemical impedance spectroscopy in alkaline solution. Impedance data analysed by equivalent circuit and mechanism for $Ni(OH)_2$ has been suggested. Formation of compact oxide layer after initial increase in capacitance was observed that was attributed to strengthening the water hydrogen bonding to nickel.

2.1 Experimental

2.1.1 Chemicals and Materials

The working electrode was nickel wire (0.5 mm diameter, Sigma-Aldrich, 99.9% purity) sealed in heatshrink teflon tubing with about 0.6 cm exposed to the solution. The electrolyte was 0.5 M KOH prepared from semiconductor grade KOH (Sigma Aldrich, 99.99%) and Millipore Milli-Q water .

2.1.2 Electrochemical Measurements

Measurements were carried out in a three electrode cell using a reversible hydrogen reference electrode (RHE) and a platinum wire counter electrode. The electrolyte was purged with Ar for at least one hour before starting the experiments and bubbled with Ar during the experiments. A Gamry Ref 600 potentiostat was used for all measurements. In the dEIS experiments, the potentiostat was run in analog mode, with the sweep and multisine signals generated and analyzed as described in Chapter 1.

Dynamic EIS

The AC signal, consisting of 45 sine waves in the range between 1 Hz - 13 kHz and with amplitudes chosen based on Popkirov's 2:10 scheme, was applied to the system while sweeping the DC potential or during a chronoamperometry experiment.

DC potential is produced by a function generator (HB-111 Hokuto Denko Ltd.). Digital to analog conversion (DAC) was performed using a Keithley KUSB-3116 ADC/DAC converter and the data was collected using a gamry potentiostat.

The lowest possible frequency for the experiments is limited by the sweep rate due to the fact that every sweep rate has a different time scale and also the lowest

frequency is chosen as the baseline for doing fast Fourier transform for all the other frequencies. The coverage should not change so much in the time scale of the lowest frequency, so, at higher sweep rates higher minimum frequency should be chosen to satisfy that. We chose 1 Hz as our minimum frequency for 5 mV s^{-1} experiment to satisfy those conditions [38].

Electropolishing

The Ni electrode was electropolished before each experiment to remove any preexisting oxide layers and ensure a clean surface for the experiments. This step consisted of applying a constant current of 1.8 A/cm^2 for 10 s in phosphoric acid (50% V/V). After electropolishing, the Ni wire was rinsed with water and transferred to the experimental cell minimizing the time out of potential control. The electrode was then conditioned using the method of Alsabet et al [55]: (i) the potential was held at -0.2 V for 200 s to reduce any remaining oxides and oxides that may be produced by the water rinse, and (ii) the potential was held at 0 V for 50 s to achieve steady state, and remove the hydride made in the first step. The electropolishing and conditioning helps to get rid of initial background anodic or cathodic currents and helps to see more pronounced peaks compared to previous reports [33].

Unelectropolished electrodes have higher cathodic currents; in the forward going cycle, in the HER region (-0.2 V to 0 V). This higher current is related to both higher HER activity and reduction of nickel oxide species [35]. Previous reports had observed anodic current at potentials between 0 V and 0.2 V, just before nickel hydroxide peak [33]; this feature is absent in our voltammograms. This feature was attributed to desorption of hydrogen that was absorbed in nickel, but in our case the hydrogen is likely removed in the conditioning step at 0 V. In our experiment, a higher anodic current at this potential range was only observed for electrodes that were polarized to higher potentials (> 1 V). Assignment of this charge to oxidation of absorbed hydrogen would then be because the HER activity is higher for electrodes

polarized to high potentials, with more hydrogen absorption accompanying the HER. Also it can be partially related to oxidized surface that is probably more active in water adsorption that increases the rate of Volmer step ($H_2O+e^- \rightarrow H(ads)+OH^-$).

Electrochemically active surface area

Measuring the active surface area is important in electrochemistry. In the case of platinum electrodes, there are well-defined hydrogen adsorption and desorption peaks, and with the assumption of one adsorbed H per Pt surface atom, the charge for an ideally flat polycrystalline surface is assumed to be 220 μC cm^{-2}. Therefore the Electrochemically Active Surface Area (ECSA), can be estimated be dividing the charge involved in hydrogen adsorption by 220 μC cm^{-2}. In the case of nickel, there are no well-defined hydrogen adsorption peaks and determining the ECSA is difficult. Jerkiewicz used the anodic charge in the nickel to nickel hydroxide oxidation region up to 0.5 V for estimation of ECSA [55], using a fairly fast sweep rate of 50 mV s^{-1} to avoid slower unwanted processes contributing to the charge. The charge was then divided by 514 μC cm^{-2}, close to the charge required for one monolayer of nickel hydroxide assuming two electrons per nickel on an unreconstructed Ni(100) surface (the value for Ni(100) is 516 μC cm^{-2}, weighted average for all the planes is 514 μC cm^{-2}). For ideal unreconstructed single crystal surfaces, two electrons per nickel atom gives 364, 516 and 596 μC cm^{-2}, respectively for the (110), (100) and (111) planes as reported by Beden [56]. The polycrystalline Ni used here will have a mix of grains of different orientation exposed to the electrolyte, and the 514 μC cm^{-2} value is an estimated weighted average. This approach also neglects the fact that unit cell parameters for bulk oxides or hydroxides are larger than for the pure metal. Additionally, it neglects any contribution from hydrogen desorption or oxygen reduction reactions that may also be occurring. Lastly, there is uncertainty in the potential where one monolayer of oxide is produced, which is also sometimes a function of sweep rate.

Hall et al. used oxalate adsorption to find the ECSA. They assumed NiOOH

formation was limited to just one monolayer after oxalate adsorption, and used the nickel oxyhydroxide to nickel hydroxide reduction charge to obtain the surface area [57].

Seyeux, using the ion density of 1.14×10^{15} (obtained from the crystal structure) in nickel hydroxide and calculated the charge required for growth of one monolayer of nickel hydroxide to be 367 μC cm^{-2}. They observed growth of 1.6 monolayers until around 0.5 V [58].

Determination of the double-layer capacitance by impedance spectroscopy in the double-layer potential region can also be used for estimating the ECSA, commonly using a value of 25 μF cm^{-2} for a smooth nickel surface [59]. However the capacitance for the oxidized surface is different than this value and can be higher or lower depending on how hydrated it is. Due to uncertainties about this value and the requirement for electrodes without roughness (generally single crystals) for accurate measurement of the calibration value, we did not use this method for our surface area calibration.

Although 514 μC cm^{-2} was used for charge correction, it is difficult to certainly assert that just one monolayer has been produced as has been discussed by [60], who observed values as high as 6.5 monolayers depending on preparation conditions. They observed an increase in reduction charge on increasing the upper limit potential for voltammograms.

Despite its imperfections, the Jerkiewicz method has been widely used in the literature and gives values not too different from most other methods, and was adopted here. Specifically, the anodic charge at 50 mV s^{-1} to 0.5 V, uncorrected for double layer charging and without other baseline corrections was used with a calibration value of 514 μC cm^{-2} to estimate the ECSA. All current densities here are quoted relative to this ECSA. It would be possible to correct for double-layer charging by using dEIS to find the double-layer capacitance, e.g., from data such as that in Fig. 2.7 c), but this departs from literature norms and so was not done here.

2.2 Results and Discussion

2.2.1 Voltammetry

Fig. 2.1 a) shows the voltammograms for formation and removal of α-$Ni(OH)_2$ at different sweep rates on the electropolished electrodes. The general shape of the voltammograms is similar to those previously reported [61]. At lower sweep rates, the potential where the current becomes anodic becomes more positive. A higher anodic charge and current peak is observed in the first cycle compared to the second cycle and the difference is more prominent at higher sweep rates. The higher charge for the first oxidation cycle compared to the second one was always observed and was reproducible after holding at potentials lower than 0 V, but it was still discernible after holding at 0.1 V. Charge trapping is a possible explanation; at higher sweep rates there is not enough time for the nickel electrode to relax back to its initial state during the reduction sweep. Also, the HER activity increases as the number of cycles increases, which is related to the nickel oxide content on the surface.

Fig. 2.1 b) demonstrates CV for wider range of potentials from -0.2 V in the HER region, to 1.8 V in the OER region. The peak around 1.4 V is for oxidation of $Ni(OH)_2$ to NiOOH. Ni oxidation to α-$Ni(OH)_2$ is observed only in first cycle. The NiOOH formation charge is higher in the first cycle compared to second cycle, but after the second cycle the NiOOH charge increases. In the first cycle, anodic current between 0.5 V and the onset potential of NiOOH formation was observed (inset) that is absent in the second cycle; this anodic charge is around 1.5 times the charge in the α-$Ni(OH)_2$ peak, that is attributed to growth of α-$Ni(OH)_2$ and β-$Ni(OH)_2$ [55], this is probably the reason for the difference between the first and second cycle in the NiOOH region. 2.1 c) shows that for first cycles, the peak current is approximately proportional to sweep rate, but there is a deviation from this relationship for second cycles. The proportionality between peak current and sweep rate for the first cycles,

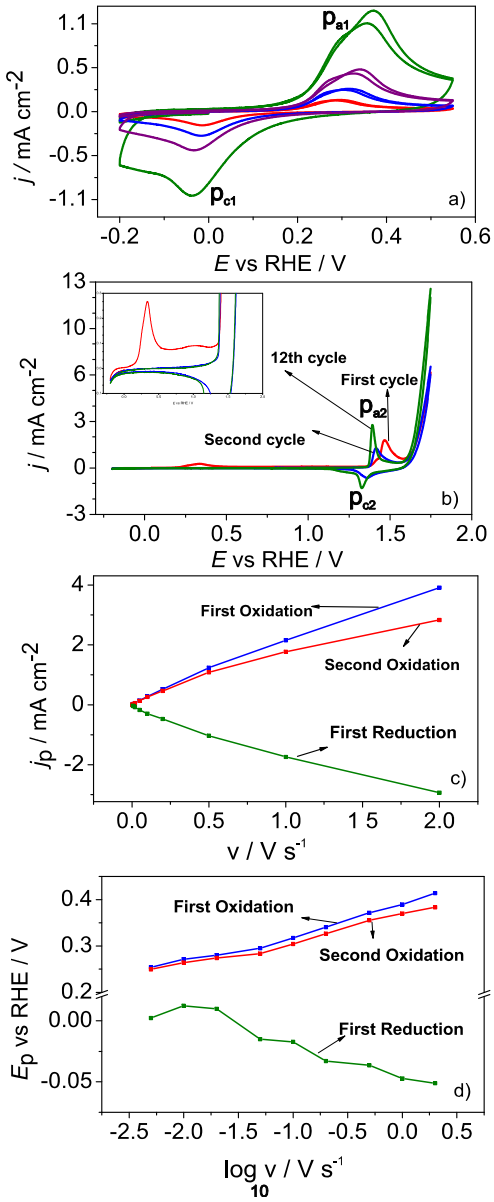

Figure 2.1: Sweep rate dependence of α-Ni(OH)$_2$ peak. a) first and second cycles of α-Ni(OH)$_2$ peak at different sweep rates (50 mV s^{-1} (red), 100 mV s^{-1} (blue), 200 mV s^{-1} (purple), 500 mV s^{-1} (green), b) Ni(OH)$_2$ and NiOOH formation potential regions, 100 mV s^{-1}, c) α-Ni(OH)$_2$ peak current at different sweep rates d) α-Ni(OH)$_2$ peak potential as a function of logarithm of sweep rate.

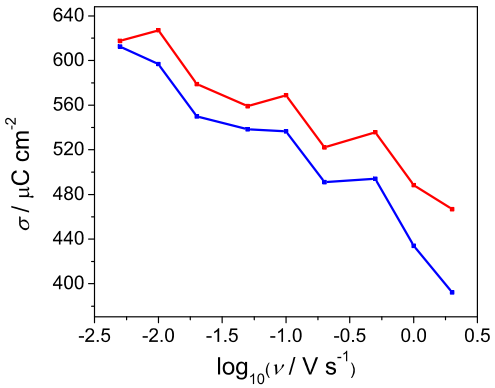

Figure 2.2: Anodic charge as a function of logarithm of sweep rate. Red: first anodic cycle, blue: second anodic cycle.

and their small change in the charge in this sweep rate range as can be seen in fig. 2.2, indicates a surface process. Charge ratio of second anodic cycle over first anodic cycle, decreases by increasing sweep rate. At low sweep rates like 5 mV/s this ratio was close to 1, then it was almost constant at 0.95 till 200 mV/s, then abrupt decrease to 0.84 at 2000 mV/s. A reason for the deviation for the second cycles may be that the reduction is slow enough that it is not complete in the first cycle, and this effect is more pronounced at the higher sweep rates.

Fig 2.1 d) shows peak potential dependence on the sweep rate. It demonstrates the increasing irreversibility of the process due to increasing the peak separation that is observed by increasing sweep rate. The slope for the the first cycle is 0.058 V, that results in α value of 1.01, based on the following equation: $2.303RT/\alpha F$=0.058. The slope for the second cycle is 0.049 V, and the resulting α value is 1.2. This value is consistent with a preequilibrium electrochemical step, possibly OH^- adsorption, before a chemical RDS. Slow electrochemical RDS with two electron transfer can result in the same α value, but it doesn't seem likely because of the presence of slow reconstruction observed in dEIS. So, as we will discuss later, fast OH^- adsorption and then a slow chemical step (possibly place exchange mechanism) is a likely guess for the oxidation mechanism. For the reduction, although the plot is not quite linear

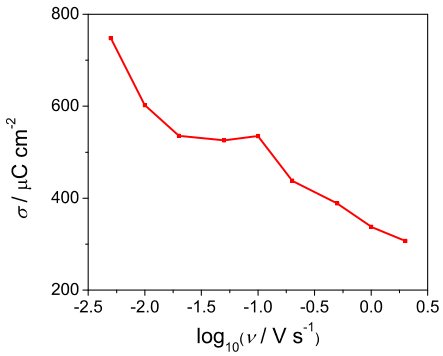

Figure 2.3: Sweep rate dependence of the reduction charge in the first cycle.

(R^2=0.92), the slope in the sweep rate range of 5 mV/s and 2000 mV/s is -0.025 V, which gives 2.3 for α, consistent with two-electron transfer preequilibrium before chemical RDS step.

The amount of $Ni(OH)_2$ made in the peak

The amount of oxide increases after each sweep because not all of the oxide produced in the anodic sweep reduces in the following cathodic sweep as it can be seen in Fig. 2.3 and 2.4. Fig. 2.3 shows almost constant reduction charge in the sweep rate range of 0.02 V s^{-1} to 0.1 V s^{-1}. The value of charge is around 500 μC cm^{-2}, that corresponds to one monolayer.

In Fig. 2.4 ratio of reduction charge to oxidation charge is less than one in sweep rates higher than 0.02 V s^{-1}. The reason for having the ratio higher than one, at 0.005 V s^{-1} is that, the reduction charge was calculated until the potential where HER current started exponential decrease (around -0.1 V vs RHE), so there is the possibilty of existence of hydrogen adsorption charge in the reduction charge. The gradual decrease in the ratio, demonstrates the slow nature of the reduction process.

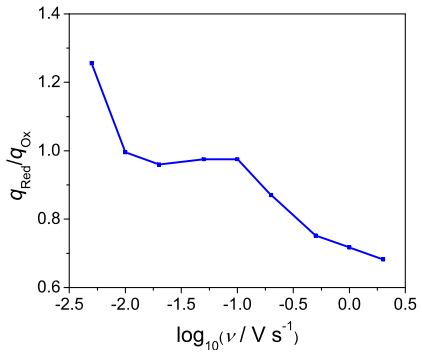

Figure 2.4: Sweep rate dependence of ratio of reduction charge over first oxidation charge.

2.2.2 dEIS

F test results

The F-test is a statistical test to determine whether or not the improved fit in adding an equivalent circuit element is statistically significant (See Chapter 1). In the α-$Ni(OH)_2$ region (0.2 V to 0.55 V), a CPE in parallel with resistance (Fig. 2.5 a)) has the best χ^2 value and also the residual errors seem to be random. For instance, fitting at the potential of 0.225 V with a capacitor in parallel with a resistor gives the value of 107.6 μF cm^{-2} for capacitance and 6750 Ω cm^2 for resistance with 15% error. The F-test confirms at the 99% confidence level that we can add a second capacitor, i.e., use capacitance in parallel with a series combination of resistor and capacitor, with double layer capacitance of 98.63 μF cm^{-2} , resistance of 2.3×10^7 Ω cm^2 and capacitance of 104.4 μF cm^{-2}. Also, the Fig. 2.5 b) circuit was allowed by the F test, but the residuals were not random. Fig. 2.5 c) had too high error for the elements, with the error of more than 40% being considered unacceptable. CPE was better than C in Fig. 2.5 a), by the F test, and it had the least χ^2 compared to the others. There were circuits like CPE in parallel with a series combination of capacitance and open Warburg that were good in terms of χ^2, but the exponent of the CPE was around 0.35 and the residuals were not quite random; this circuit was avoided because of the high

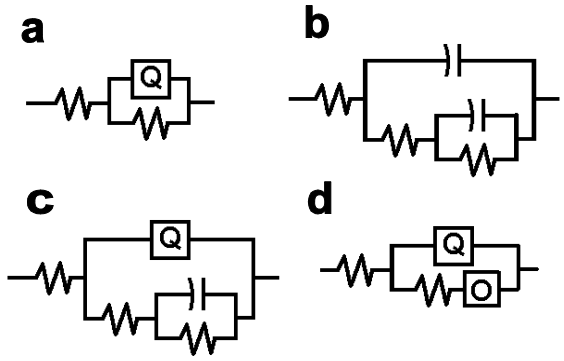

Figure 2.5: Equivalent circuits used for fitting and comparing F test results. Q is constant phase element and O is finite Warburg element, with transmittance boundary condition.

deviation of the exponent from physically reasonable values near one. Those circuits with capacitors instead of CPEs had residuals that were not quite random and high errors for the circuit components. Circuit 2.5 b) without adsorption resistance was not a good fit in the low frequency region.

In the reduction region at potentials around -0.087 V after potential holding experiments at 0.5 V, adding more elements was allowed by the F test. Comparing circuits 2.5 c) and 2.5 d) that have the same number of parameters, circuit 2.5 d) had a lower χ^2, 0.00061 compared to 0.000797. Circuit 2.5 a) had χ^2=0.0033 at this potential.

Circuit 2.5 a) was chosen to fit all the results due its low χ^2, randomness of residuals and low error for circuit components, and in order to compare the results at different potentials. This is the same circuit as used by Hall et al in a study of the effect of NiH on decrease in HER activity [33].

Fig 2.6 shows the Nyquist and capacitance plots used for simulating some ideal cases that had close parameters to our actual impedance data. Using capacitance plots has the advantage of seeing more features that sometimes are difficult to see in Nyquist plots.

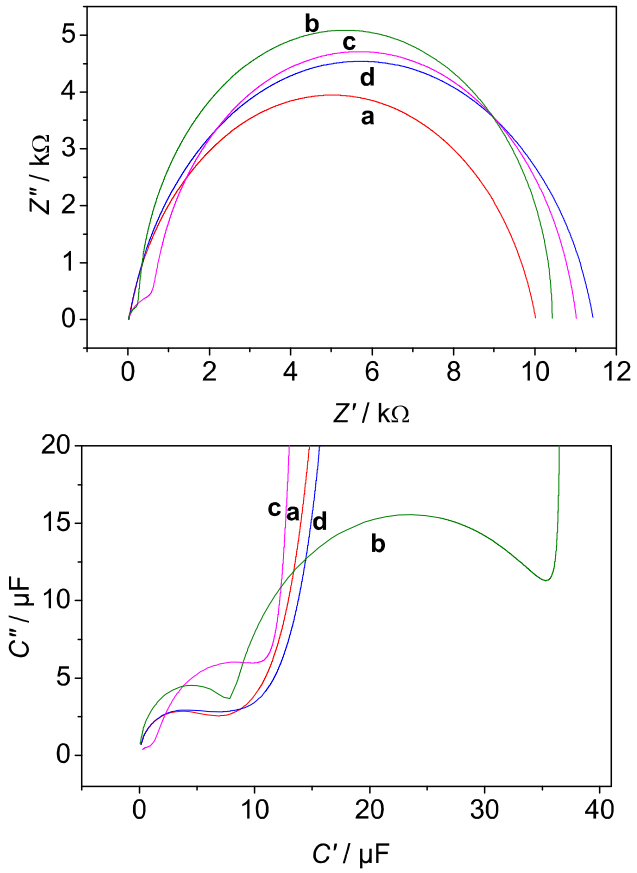

Figure 2.6: Comparison of Nyquist and capacitance plots. Parameters for each circuit: R_s=21 **a)** R_{ct}=10000, Y_{CPE}=$2\times10^{-5}(i\omega)^{0.85}$ **b)** R_{ads}=10000, C_{ads}=3×10^{-5}, R_{ct}=400, C_{dl}=9×10^{-6} **c)** R_{ads}=10000, C_{ads}=1×10^{-5}, R_{ct}=1000, Y_{CPE}=$7\times10^{-6}(i\omega)^{0.8}$ **d)** Y_O=$1.4\times10^{-5}(i\omega)^{0.5}\coth(0.15\times(i\omega)^{0.5})$, R_{ct}=700, Y_{CPE}=$2\times10^{-5}(i\omega)^{0.85}$

Sweep-Hold-Sweep Results

In order to study the potentiostatic growth of the α-Ni$(OH)_2$ and its interconversion to β-Ni$(OH)_2$, the potential was held at two selected potentials, 0.25 V and 0.5 V. There are three possibilities as a consequence of holding: decrease in reduction charge that could mean conversion of α-Ni$(OH)_2$ to β-Ni$(OH)_2$, no change in reduction charge meaning no aging at these potentials, and an increase in charge (observed here for 0.5 V) meaning continued growth of an oxide layer possibly with simultaneous occurrence of the α to β transformation. Fig. 2.7 a) shows the voltammograms obtained before and after holding. After holding at 0.5 V, an increase in reduction charge, and shift of reduction potential to more negative potentials, is observed. After holding at 0.25 V, a decrease in reduction charge compared to a regular CV without a hold period is observed. The anodic charge after holding is almost the same, indicating supposedly no α to β conversion; in agreement with reported onset potential for α to β transformation (0.23 V vs Ag/AgCl ,0.9 V vs RHE at pH 8.4) [36, 37]. The shift of the reduction peak potential to more negative potentials and mixing with HER region can be explained by transformation of α-Ni$(OH)_2$ to β-Ni$(OH)_2$, with stronger nickel and oxygen bonding and delocalized hydrogen bonds to Ni-O that results in lower interlayer spacing and causes dehydration of interlayer spacing, but it is not consistent with EQCM experiments [62]. Although the onset potential for reduction is the same and the process happening seems to be the same, with the only difference in amount of oxide that is been reducing, the shift in reduction peak potential clearly can be seen. Considering the fact of low sweep rate, we relate this shift to more negative potential to strengthening NiO bond or stronger hydrogen bonding between intercalated water and nickel. Both these explanations can be true, but possibly strengthening hydrogen bonding is the more probable reason. Also, there is the possibility for some intermediate phases to be involved in this process. Oshchepkov observed an increase in HER activity on increasing the amount of oxide on the surface [63]; here we attribute the increase in reduction charge by holding at

0.5 V, mostly to reduction of $Ni(OH)_2$. Although slow desorption of water will lead to same decrease in capacitance, and may seem likely because of compression forces on non hydrogen bonded regions, this effect is not prominent because of an increase in mass (8 g mol^{-1} until 0.5 V, and further increase by sweeping to more positive potentials) is observed in EQCM [62] consistent with adsorbing water and hydrogen bonding.

Holding at 0.25 V resulted in higher steady state capacitance than when the surface was cycled to 0.55 V or held at 0.5 V. This shows that the process is slow at 0.25 V and the need for higher potential for complete oxidation. There is the possibility for hydrogen absorption by holding at -0.2 V, but we assume all the anodic charge goes to nickel surface oxidation, because the hydrogen desorption contribution to overall charge is small. This is established noting that anodic charge is almost the same in all the sweep rates.

The possible explanation for seeing a higher reduction charge after holding at 0.5 V can be formation of more than one monolayer of oxide. This reduces hydrogen adsorption activity of the electrode as shown in the capacitance plot where the increase in capacitance happens at around 0.1 V, while without holding, the increase in capacitance occurs at higher potentials, around 0.2 V, that can be related to water adsorption.

Fig. 2.7 b) shows R_{ct}^{-1} obtained by fitting the impedance data. In theory extrapolating R_{ct}^{-1} to the frequency of zero should give the slope of steady state current, so by comparing the dj_{ss}/dE and R_{ct}^{-1} we can get the idea about rate of different processes and see if we are missing any slow process in lower frequencies. we are plotting current and potential in slow sweep, 5 mV s^{-1}, so the real steady state has not been completely established. in HER region these two plots are close to each other, as we get close to nickel oxidation region, dEIS predicts lower resistance than slope of current potential, it can be related to slower process with higher time constant that we can not see in our dEIS experiment. For example, if the process consists of another

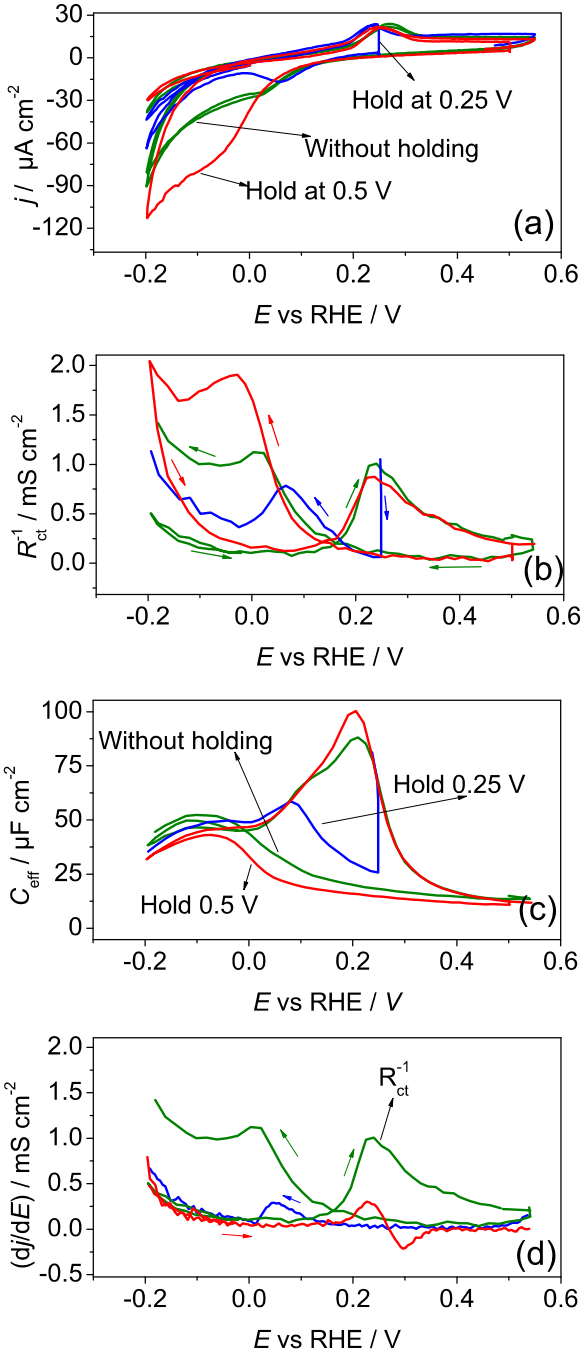

Figure 2.7: Sweep-hold-sweep experiments. a) CV at 5 mV s^{-1} interrupted with potential hold periods, green: without hold, blue: hold at 0.25 V and red: hold at 0.5 V, b) simultaneous measurement of R_{ct}^{-1}, c) C_{eff}, d) comparison of (dj/dE) and R_{ct}^{-1} without holding, red: dj/dE for forward sweep, blue: dj/dE backward sweep and green: R_{ct}^{-1}.

adsorption step so that the equivalent circuit would be parallel combination of double layer capacitance with series combination of charge transfer resistance and parallel combination of capacitance and resistance. If the charge transfer resistance is small the capacitance that we are measuring would be sum of double layer charging and adsorption capacitance, this can justify the high capacitance during oxide formation. Sweep and hold at more positive potentials shifts the peak in the reduction sweep to more negative potentials. Fig. 2.7 c) demonstrates effective capacitance that was calculated by fitting the data, and using Brug equation [64],

$$C_{\text{eff}} = \left(Y_0 (R_{\text{s}}^{-1} + R_{\text{ct}}^{-1})^{n-1} \right)^{1/n} \tag{2.1}$$

where R_{s} is the solution resistance, R_{ct} is the charge transfer resistance and Y_0 and n are parameters of the constant phase element. The admittance of a constant phase element can be written as Eq. *2.2*, Y_0 is admittance of CPE and n exponent factor for CPE. C_{eff} as a function of potential can be used as a measure of double layer charging, which could be used to make a correction for accurate charge measurement for the oxide region. However it may be a mixture of double layer charging and capacitance of the oxide layer. At the lower potentials (lower than 0.25 V) where there is only submonolayer growth, double layer capacitance and oxide layer capacitance are in parallel, but in more positive potential where possibly at least one complete monolayer of $Ni(OH)_2$ has grown on the surface, this layer is in series with the double layer capacitance, which leads to a decrease in total capacitance.

$$Y_{\text{CPE}} = Y_0 (\mathrm{i}\omega)^n \tag{2.2}$$

As it can be seen in fig. 2.7 d) in the potential range of -0.2 V to 0 V in the forward scan, the charge transfer resistance derived from the impedance experiment and $\mathrm{d}j/\mathrm{d}E$ are in good agreement, and the process happening in this region is hydrogen evolution reaction. In the potential region 0 V to 0.25 V fitting shows lower charge transfer

resistance but actual charger transfer is higher. This means that there are slower processes that would appear at frequencies lower than the dEIS limit of 1 Hz. These slower processes can have several characteristic semicircles that leads to an increase in polarization resistance that is the zero frequency limit in dEIS. In the 0.25 to 0.3 V that corresponds to slightly before the peak to the end of the peak, the R_{ct} keeps decreasing in impedance but increases in CV, becomes infinity at the peak and then keeps going to negative values. In impedance in the frequency range that was used, there is access to rate of intermediate steps of the reaction, the rate of the intermediate steps was increasing in this region (probably OH adsorption step) but the rate of RDS was decreasing.

The differences between α-$Ni(OH)_2$ and β-$Ni(OH)_2$ is interlayer spacing and presence of free water in α-$Ni(OH)_2$, but there is no difference in their first monolayer that consists of nickel layer that is sandwiched between two OH layers, so the first formed oxide can be considered to be α or β.

Structural rearrangements happens during holding, water diffuses to the surface and probably desorbs and leaves a dehydrated structure.

Oblonsky studied passive film formation on nickel in the potential region of after nickel hydroxide formation and before NiOOH onset potential, using surface enhanced Raman spectroscopy, they observed broader peaks compared to their reference compounds that attributed to amorphous or semicrystalline nature of passive film. They attributed shifting the NiOH lattice mode from 318 cm^{-1} to 380 cm^{-1} to strengthening nickel and oxygen bond compared to bulk nickel hydroxide, also shifting down in OH stretching from 3580 to 3510 was attributed to weakening oxygen and hydrogen bond [65], so proton delocalisation in initially formed $Ni(OH)_2$ after the holding can be the reason for capacitance drop in fig.2.7.

There are three processes that occur in the system. In order to have more accurate charge measurement, each of these processes should be disentangled. The first process

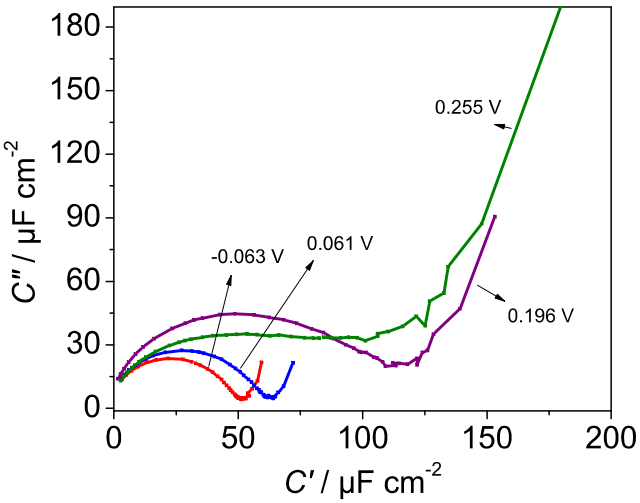

Figure 2.8: Capacitance plots at different potentials

is double layer charging; the charge required for this process was obtained by fitting the impedance spectra by the circuit shown in fig 2.5 a) and calculating the effective capacitance using resulting values for the charge transfer resistance and constant phase element. In the capacitance plot, the decrease and plateau is due to capacitive discharging because of the hydrogen evolution reaction and not double layer charging. Small values of capacitance and small coverage changes in the HER region that is almost in the range of double layer charging suggests that water adsorption and dissociation (Volmer step) is the rate determining step in the HER, in agreement with previous reports [66, 67]. If Tafel step was RDS, it would increase adsorbed hydrogen coverage and as a result increase in capacitance

Fig. 2.8 shows capacitance plots derived from impedance spectra. In this plot features are more distinct than in the Nyquist plot. The increase in constant phase element, the initial increase in charge transfer resistance from -0.065 V to 0.061 V, and then the decrease at 0.255 V can be observed.

Fig. 2.9 shows that although steady state capacitances are different the time constants for the process at 0.25 V and 0.5 V are close to each other. The time

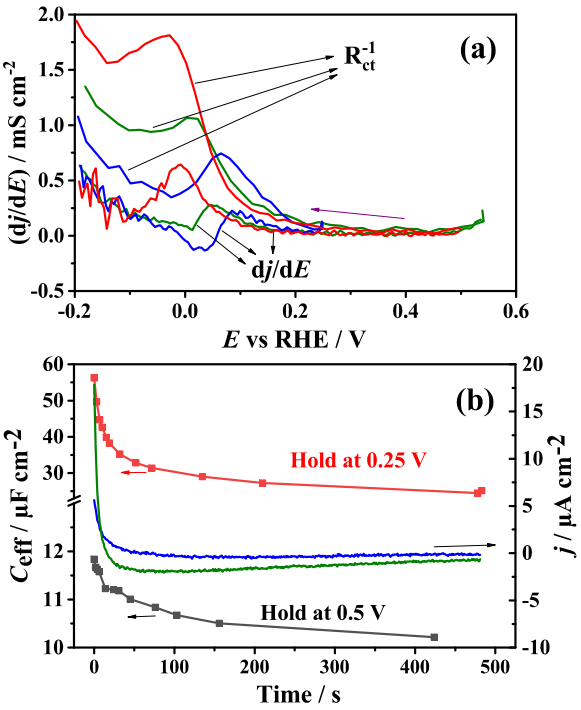

Figure 2.9: Top: Slope of voltammograms in reduction region, comparing R_{ct}^{-1}, blue: hold at 0.25 V, green: without hold and red: hold at 0.5 V. Down: Effective capacitance and current density change during potential holding. Green: current 0.25 V, blue: current 0.5 V, red: capacitance 0.25 V, black: capacitance 0.5 V.

constant obtained from impedance in Fig. 2.10 is lower than the time constant of capacitance change during hold, that indicates slower reconstruction of the surface.

Fig. 2.11 shows how the Nyquist plot changes during the hold period. The charge transfer resistance (diameter of semicircle) increases with time.

Admittance plots Fig. 2.12 shows the admittance at different frequencies that are characteristic of processes with different rates. At 52 Hz initially at small overpotentials of HER, admittance does not change, then sweeping to more negative potentials decreases the admittance. The lower admittance at 900 Hz in the backward sweep in the potential region for hydrogen adsorption (lower than 0.2 V) is related to decrease in adsorption energy of hydrogen to nickel, so introducing an oxide layer will

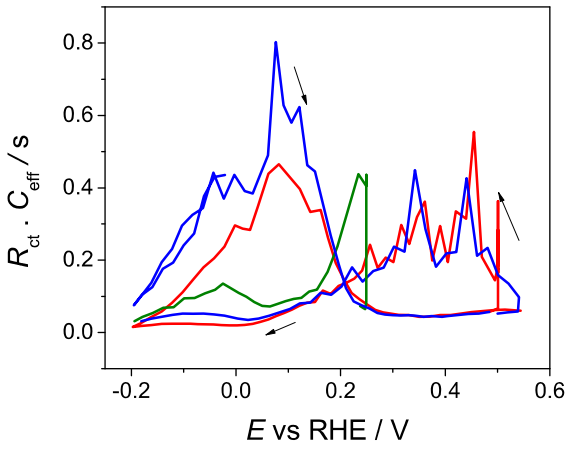

Figure 2.10: Time constants obtained using elements of circuit a. Sweep rate: 5 mV s^{-1}, green: hold at 0.25 V, blue: without hold and red: hold at 0.5 V.

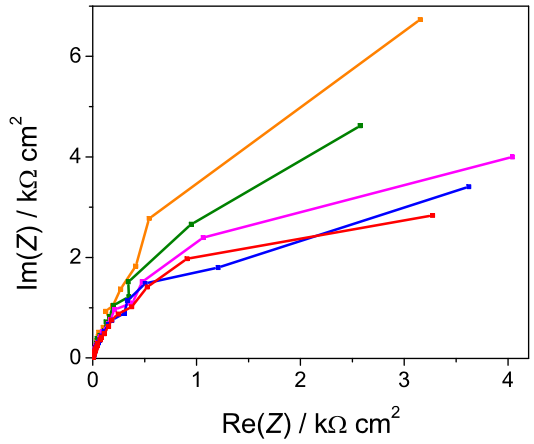

Figure 2.11: Nyquist plots during the hold. Red: after 1 s Blue: after 3 s Magenta: after 7 s, Green: after 17 s, Orange: after 117 s.

decrease the rate of Volmer step. This can be seen in admittance at 1 Hz, where the increase in admittance for HER is shifting to more negative potentials. However, it will lead to an increase in the rate of the Tafel step, it is not observed here at the low overpotentials (-0.2 V).

Comparing the admittance plots at 3 Hz and 52 Hz it can be seen that the ratio between oxidation and reduction admittance is almost the same. At 3 Hz in the potentials lower than 0 V, the increase in admittance can be related to the HER. At 52 Hz, there is no increase in this region, which suggests that the HER is slow and is limited by coverage of hydrogen on the electrode. Comparing the admittances at 1 Hz and 3 Hz, it is clear that the reduction process is faster when potential holding is 0.25 V. Higher admittance at 1 Hz for holding at 0.5 V and regular CV confirms lowering the rate of reduction.

An increase in admittance is observed from about 0 V, before the onset potential for oxidation that is observed in CV. It can be attributed to dissolution of step edges and nucleation of the oxide layer [58]. The low rate of retraction of step edges reported in [58] at onset potentials of nickel oxide formation is in agreement with our observed low charge after holding at 0.25 V. At 0.5 V it is not limited by dissolution and probably the rate of nucleation is high, so the rate of place exchange mechanism can be considered as rate limiting at this potential.

OH adsorption starts before onset and because the potential is close to PZC the bonding between OH and nickel is weak that leads to the higher capacitance that is observed. Adsorbed OH groups have fast surface diffusion that are stabilized by sweeping to more positive potentials which, strengthens the bonds by reaching to more favorable thermodynamic conditions.

Fig. 2.13 shows that starting from -0.2 V initial increase in imaginary part of impedance of 1 Hz occurs that follows by decrease until onset potential of nickel oxidation then almost linear increase after that. In reduction, decrease in imaginary

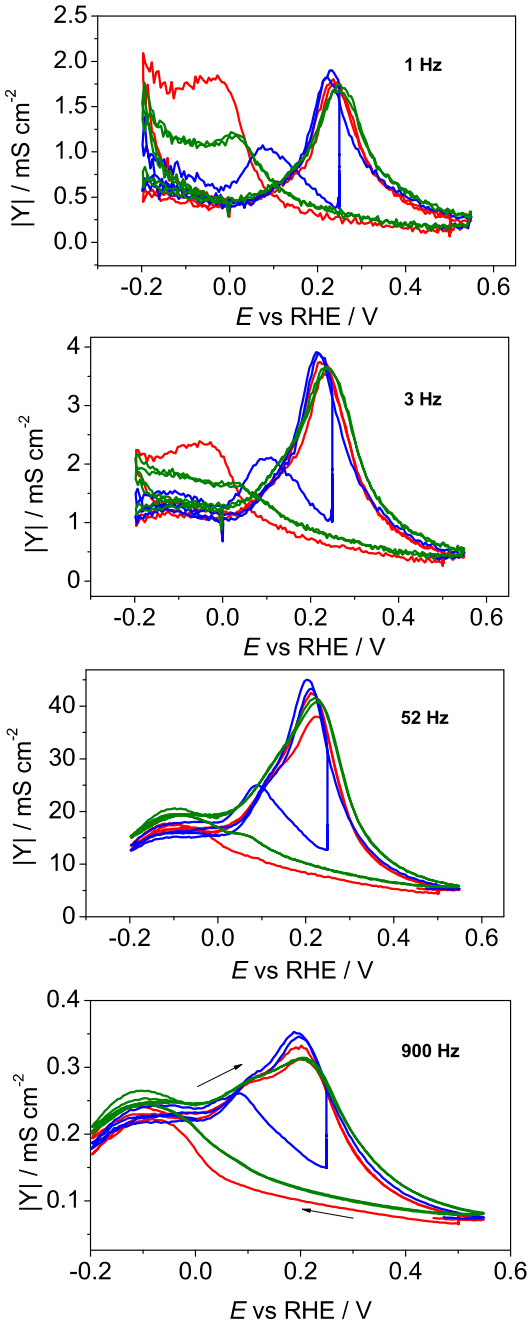

Figure 2.12: Admittance plot at different frequencies at 5 mV s^{-1}, green: without holding, blue: hold at 0.25 V and, red: hold at 0.5 V.

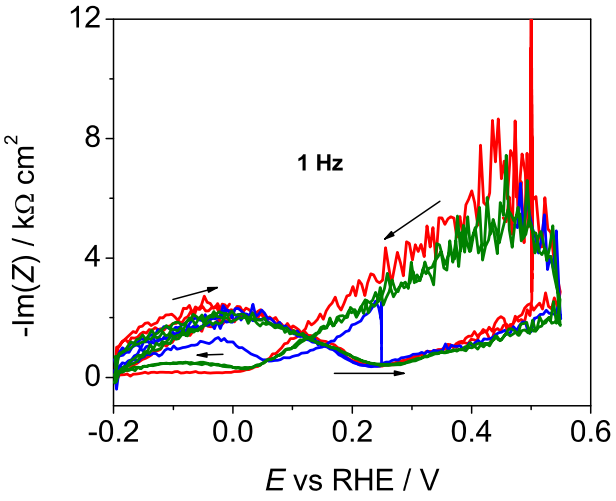

Figure 2.13: Imaginary part of impedance at 1 Hz, at different holding potentials. Green: without holding, red: hold at 0.5 V, blue: hold at 0.25 V.

part was observed until around 0 V, then it stays constant.

Lower capacitance in 0.5 V compared to 0.25 V holding is related to lower thickness in 0.25 V (in holding at 0.25 V, it is submonolayer and in holding at 0.5 V, three or four monolayers) because of lower rate of oxidation. Possibly at 0.25 V it is initially hydrated that by holding dehydrates and possibly produces compact layer that seems to be different in nature than the one produced in 0.5 V.

Until around 0.7 V increase in reduction charge and peak is observed, also reduction peak potential is shift to more negative potentials, at 0.8 V the shape is different, there is no clear reduction peak and it is mixed with HER. going to higher potential the shape of reduction is almost same as 0.8 V, also decrease in oxidation charge after going to 0.8 V and higher potentials is observed (not shown here).

Sweep-hold at 0.29 V Fig 2.14 shows the potential program applied to the electropolished system, and the results are discussed in the following graphs.

Fig. 2.15 shows the phase as a function of potential. Between 0 V and 0.030 V there is a region where the phase is at its maximum and the impedance shows almost

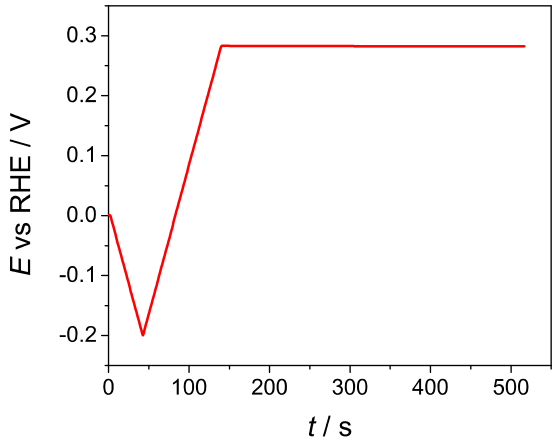

Figure 2.14: Potential program used for the experiment in 0.5 M KOH solution.

a capacitive behaviour; this region can be estimated as the double layer region, where no charge transfer reaction occurs and the adsorption or change in coverage is without electron transfer.

Fig. 2.16 shows how the admittance changes during the experiment, specifically during the hold period.

Fig. 2.17 shows the admittance at 5200 Hz, which is attributed to double layer charging and the surface condition. The decrease in capacitance corresponds to formation of the oxide layer.

Fig. 2.18 shows the imaginary part of impedance at 5200 Hz, corresponding to the previous plot (admittance at 5200 Hz).

As can be seen in Fig. 2.19, during the hold period the imaginary part of the impedance shows a higher time constant than the real part (it took more time for the imaginary part to reach the pseudo steady state value).

In terms of the mechanism for oxide formation, Seyeux et al. [68] observed nickel hydroxide formation and simultaneous dissolution at step edges. They observed

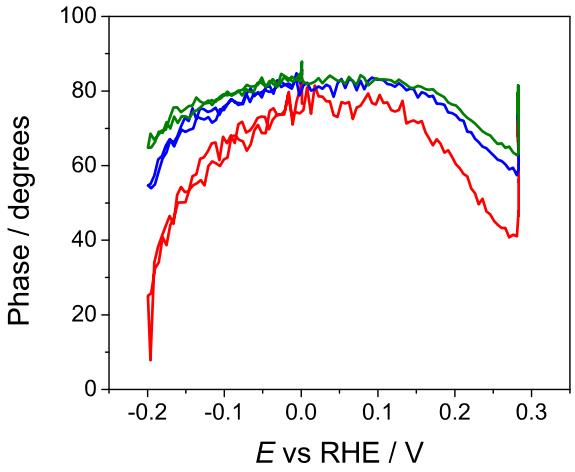

Figure 2.15: Impedance phase at different frequencies as a function of potential, holding at 0.3 V, sweep at 5 mV s^{-1}. Red: 1 Hz, blue: 3 Hz and green: 5 Hz.

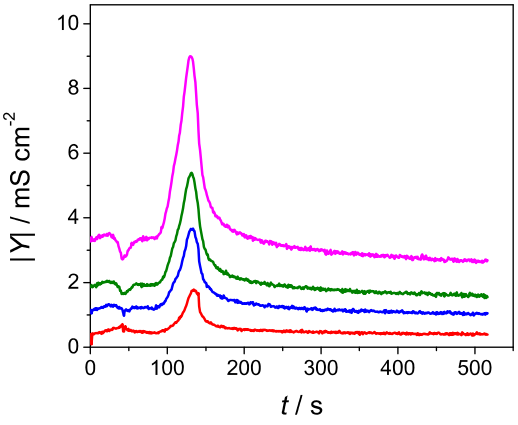

Figure 2.16: Admittance as a function of time for sweep hold to 0.29 V, sweep at 5 mV s^{-1} (as in Fig. 2.15) Red: 1 Hz, blue: 3 Hz, green: 5 Hz and magneta: 9 Hz.

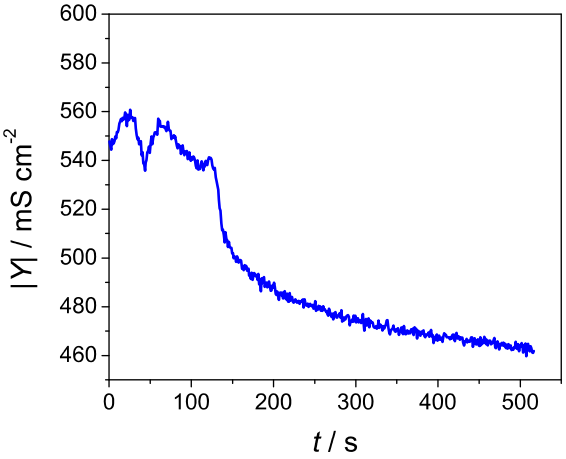

Figure 2.17: Admittance at 5200 Hz for sweep hold to 0.29 V.

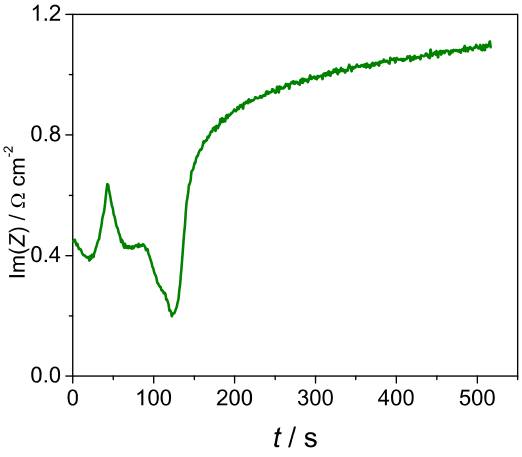

Figure 2.18: Imaginary part of impedance at 5200 Hz.

1 3hz

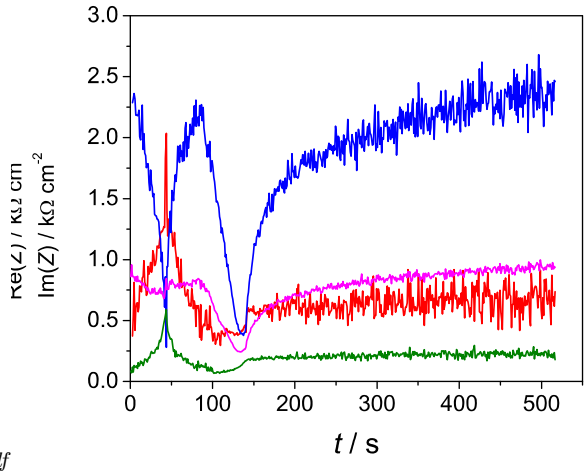

$_{2}$5.*pdf*

Figure 2.19: Real and imaginary part of impedance as a function of time for holding at 0.29 V experiment. Red:real 1 Hz, blue:imaginary 1 Hz, green: real 3 Hz, and magneta: imaginary 3 Hz.

roughening of the surface in the corroded areas, and found that the corroded areas were separated with areas that were resistant to dissolution because of formation of 2D oxide layer.

2.2.3 Effect of KOH Concentration

Fig. 2.20 shows the voltammogram in 0.1 M KOH solution; the trend and shape of the CV is similar to that in 0.5 M. Holding at higher potentials results in more charge in the reduction cycle.

In Figs. 2.21 and 2.22 higher admittance and lower current for holding at 0.2 V, compared to holding at higher potentials demonstrates that the rate of reduction decreases (reduction becomes more difficult) by holding the potential and growing the oxide layer at more positive potentials.

Based on the admittance plot at 3 Hz (Fig. 2.22), the reduction is slightly faster in 0.1 M KOH compared to 0.5 M KOH (Fig. 2.12).

The admittance at 52 Hz in Fig. 2.23 shows the same trend as the admittance at

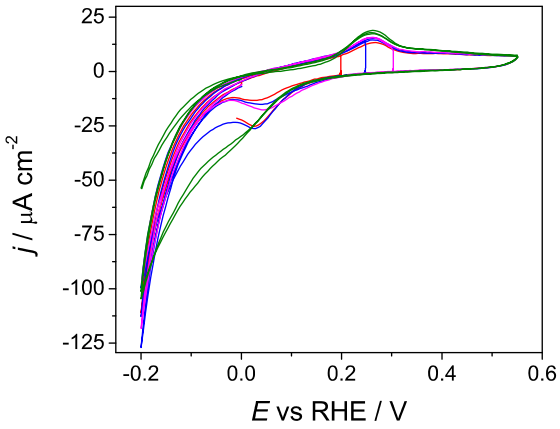

0.pdf

Figure 2.20: Voltammograms for the sweep-hold experiments in 0.1 M KOH solution at 5 mV s^{-1}.

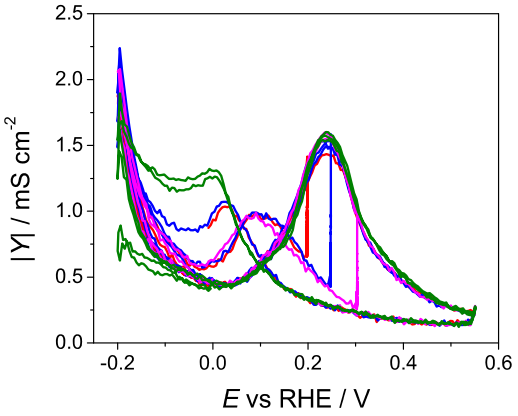

Figure 2.21: Admittance at 1 Hz in 0.1 M KOH and 5 mV s^{-1}.

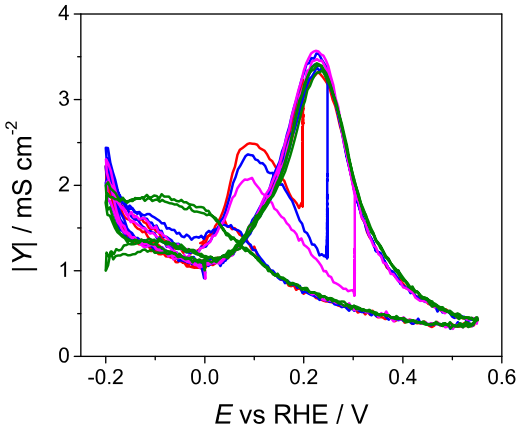

Figure 2.22: Admittance at 3 Hz in 0.1 M KOH and 5 mV s^{-1}.

lower frequencies. The experiment without holding shows no peak in the reduction region and there is a clear shift to more negative potentials, which demonstrates the lower rate of reduction by going to more positive potentials.

Real and imaginary parts of the impedance at 1 and 3 Hz are shown in Fig. 2.24.

The effective capacitance in Fig. 2.25 in the backward sweep at the peak potential, shows a slightly higher value for hold at 0.2 V. However, at more negative potentials, the effective capacitances are the same, which shows that more negative potentials were needed to reduce the oxide when the holding is at more positive potentials (at 5 mV s^{-1}).

Fig. 2.26 shows that the half life for the capacitance decay at 0.2 V is around 75 s, and for 0.25 V, around 13 s.

Fig. 2.27 shows the result of data fitting. It can be seen that R_{ct}^{-1} is higher for the hold at 0.25 V, which is contrary with the admittance plots (Figs. 2.21 and 2.22). The explanation is that, the slower processes occurring during the reduction are missed.

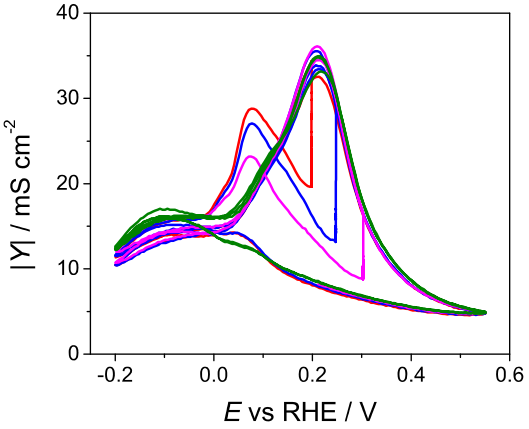

Figure 2.23: Admittance at 52 Hz in 0.1 M KOH and 5 mV s^{-1}.

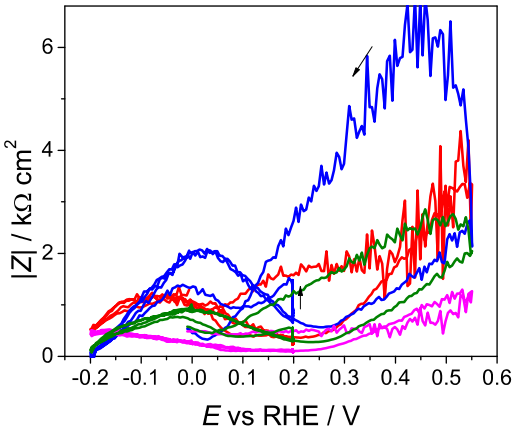

Figure 2.24: Real and imaginary parts of impedance at 1 and 3 Hz in 0.1 M KOH. Red: real 1 Hz, blue: Im 1 Hz, magenta: real 3 Hz, green: Im 3 Hz

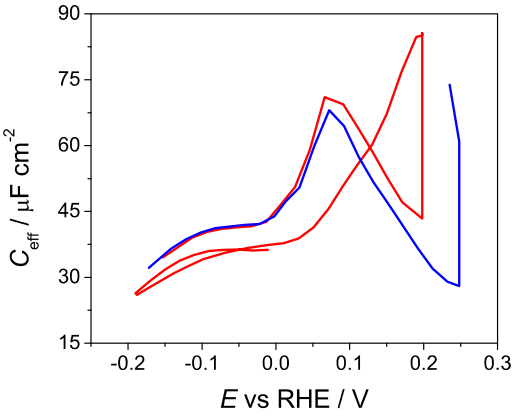

0.pdf

Figure 2.25: Effect of potential hold on effective capacitance in 0.1 M KOH.

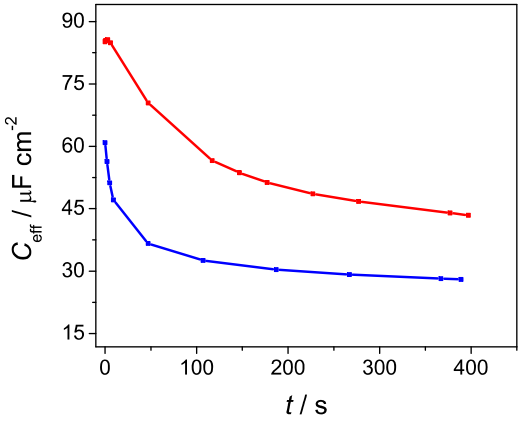

Figure 2.26: Effective capacitance change during the hold in 0.1 M KOH. Red: 0.2 V, and blue: 0.25 V.

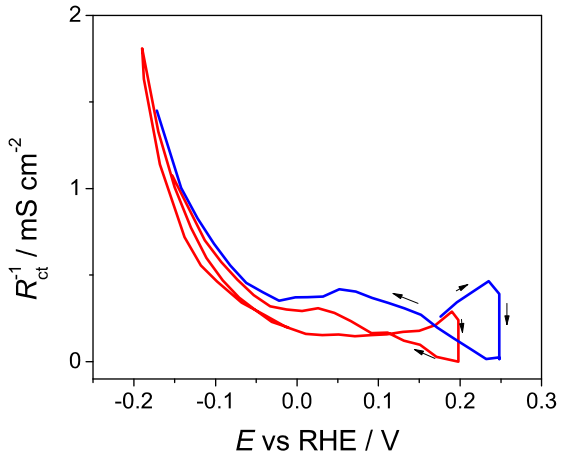

Figure 2.27: R_{ct}^{-1} dependence to holding potential in 0.1 M KOH.

2.2.4 Mechanism of the electrooxidation

The following reactions can be involved in nickel hydroxide formation.

$$\mathrm{Ni+OH^- \leftrightarrow NiOH(ads)+e^-} \tag{2.3}$$

$$\mathrm{NiOH(ads) \rightarrow OHNi(ads)} \tag{2.4}$$

$$\mathrm{OHNi(ads) + OH^- \rightarrow Ni(OH)_2 + e^-} \tag{2.5}$$

$$\mathrm{Ni+OH^- \rightarrow NiO(ads)+H^+ +2e^-} \tag{2.6}$$

$$\mathrm{Ni+2OH^- \rightarrow NiO.H_2O(ads)+2e^-} \tag{2.7}$$

$$\mathrm{Ni(OH)_2 \rightarrow NiO.OH^-(ads)+H^+} \tag{2.8}$$

$$H_2O(ads) \rightarrow O^{2-}(ads)+2H^+ \quad (2.9)$$

$$2OHNi \rightarrow 2NiO+2H^++2e^- \quad (2.10)$$

Eqs. 2.8 and 2.11 are the possible chemical reactions after $Ni(OH)_2$ formation, that stabilize the surface. Thicker passivated layer reported at higher pH can be related to more adsorbed water involved, that is required to stabilize repulsions for OH^- that is higher in higher pH. Water dissociation to oxygen anion (2.9) probably does not occur at this potential due to its high energy requirement.

$$Ni(OH)_2+OH^- \rightarrow NiO.H_2O(ads).OH^-(ads) \quad (2.11)$$

The kinetics for the mechanism of Eqs. 2.3-2.5 are given by

$$\nu_1 = k_1\,\theta_{Ni}\,\exp(\frac{\beta F}{RT}\eta) - k_{-1}\,\theta_{NiOH}\,\exp(\frac{-(1-\beta)F}{RT}\eta) \quad (2.12)$$

$$\nu_2 = k_2\,\theta_{NiOH} - k_{-2}\,\theta_{OHNi} \quad (2.13)$$

$$\nu_3 = k_3\,\theta_{OHNi}\,\exp(\frac{\beta F}{RT}\eta) \quad (2.14)$$

$$1 = \theta_{Ni} + \theta_{NiOH} + \theta_{OHNi} + \theta_{Ni(OH)_2} \quad (2.15)$$

But most possibly the first step is in equilibrium, so it can be rewritten as

$$K_{eq1}=\frac{\theta_{NiOH}}{\theta_{Ni}}\exp(\frac{F}{RT}\eta) \quad (2.16)$$

$$j = F\ (\nu_1+\nu_3) \tag{2.17}$$

$$\Gamma_{\mathrm{m}}\frac{\mathrm{d}\theta_{\mathrm{Ni}}}{\mathrm{d}t} = -\nu_1 \tag{2.18}$$

$$\Gamma_{\mathrm{m}}\frac{\mathrm{d}\theta_{\mathrm{NiOH}}}{\mathrm{d}t} = \nu_1-\nu_2 \tag{2.19}$$

$$\Gamma_{\mathrm{m}}\frac{\mathrm{d}\theta_{\mathrm{OHNi}}}{\mathrm{d}t} = \nu_2-\nu_3 \tag{2.20}$$

Adsorbate induced restructuring of the surface can also happen. Transformation of $\mathrm{NiOH_{ads}}$ to $\mathrm{OHNi_{ads}}$ can be due to the moving of nickel atoms.

Based on features observed in capacitance plot we conclude earliest stage of the oxidation converts strongly bounded water and hydroxide to hydrated α-$\mathrm{Ni(OH)_2}$. The initial increase in capacitance until 0.25 V can be associated with adsorption and creating the hydrated layer. Sweeping the potential to 0.5 V decreases the capacitance and holding for more time at this potential makes more than one monolayer, as observed by the slight decrease in capacitance by holding at 0.5 V. The approach for interpreting the results is based on hydrogen bonding between OH groups in nickel hydroxide and intercalated water that decreases the rotational freedom for water and leads to decrease in ε, which as a result decreases the capacitance.

Holding increases irreversibility as can be seen by the shift in the reduction to more negative potentials.

The imaginary part of impedance (Fig. 2.13) is characteristics of capacitance elements involved in the process, and valuable information about adsorption and surface coverage can be obtained by plotting the imaginary part of impedance as a function of potential. Low frequency imaginary parts are related to adsorption steps involved in rate determining steps, and high frequency imaginary parts are attributed to double layer charging

The potential of zero charge (PZC) of nickel is around 9.5 [69], so, in 0.5 M KOH

solution and at pH higher than 9.5 and before nickel oxide potential region nickel's surface is negatively charged and there is weak interaction between OH^- groups and nickel surface, by increasing the potential, nickel's surface becomes positively charged and enables adsorption of OH^- [62], as can be seen by the dramatic increase in effective capacitance before the onset potential for nickel oxidation.

Voltammograms of the admittance at low frequencies were found to be sensitive to the surface condition, and showed that the surface condition did not return to the same value after cycling.

In Fig. 2.10 the time constant has been attained by multiplying the charge transfer resistance and effective capacitance, these time constants are much lower than the values obtained from Fig. 2.9, the difference between time constants represents that there are slower processes, possibly surface reconstruction, going on, and these can only be observed by the hold experiments. It is important to emphasize that these time constants are calculated under the assumption that the process is only one semicircle in Nyquist plot (as was satisfied by statistical tests) however the real R_{p} that should be used for calculating the slower time constant is zero frequency limit of real part of impedance. Also, time constants obtained are related to the time for charging the capacitance of the oxide layer as well as double layer (Stern or Helmholtz layer) charging, because the time constant for only double layer charging is usually small. Therefore, it makes sense that this process has higher time constant in the forward going sweep (it takes more time to create this oxide layer (two or three monolayers of $Ni(OH)_2$)) than the backward sweep where the time constant is the time for charging the already formed oxide layer. For holding at 0.25 V, the time constants for current drop and capacitance drop are 4 s, and 11 s, respectively. These values for holding at 0.5 V are 7 s and around 35 s.

2.3 Conclusions

Impedance data provides insight about the initial stages of nickel oxidation. Formation of compact oxide layer, that can be hydrogen bonded α-$Ni(OH)_2$ (latter is more probable), was attributed to strengthening water bond to OH group in $Ni(OH)_2$ that leads to decrease in the ε and as a result the effective capacitance. Holding the potential at 0.5 V resulted in production of several monolayers (as observed by the increase in the reduction charge after the potential hold) and strengthening the bonds, made the reduction more difficult. The use of complex capacitance plots showed evidence for additional structure at low frequencies. Comparison of the polarization resistance determined from the slope of the voltammograms with the estimated low-frequency intercept of the impedance showed a discrepancy in the peak region, which also suggests that a slow process exists whose kinetics are not determinable by dEIS.

2.4 Acknowledgements

This research was conducted as part of the Engineered Nickel Catalysts for Electrochemical Clean Energy project administered from Queen's University and supported by Grant No. RGPNM 477963-2015 under the Natural Sciences and Engineering Research Council of Canada (NSERC) Discovery Frontiers Program.

Chapter 3

Early stages of NiOOH growth: dEIS Study

In this chapter NiOOH is grown on the surface of the nickel by sweeping the potential between 1 and 1.6 V, and is studied using dEIS.

3.1 Results and Discussion

First, $Ni(OH)_2$ to NiOOH transformation is studied as a baseline behaviour for understanding the glycerol oxidation.

3.1.1 $Ni(OH)_2$/NiOOH

Fig. 3.1 shows the oxidation and reduction peaks for transformation of $Ni(OH)_2$ to NiOOH in the potential region of 1 to 1.6 V. An oxidation peak is observed at around 1.35 V that is attributed to $Ni(OH)_2$ to NiOOH oxidation, that can include ion intercalation (Eq. 3.1). In the backward sweep the reduction signal is observed starting at around 1.45 V. The oxidation is a deprotonation step, in which $Ni(OH)_2$

protons covalently to the nickel in the OH groups are released. Cycling promotes the formation of a double peak in the reduction region and, also a higher charge in the forward cycle in the potential region of 1.45 V to 1.55 V.

Double peaks in the reduction have been seen by others [70,71]. It is either related to interconversion of different phases of $Ni(OH)_2$ and NiOOH or to iron impurities.

Due to the precautions taken to ensure the cleanliness of the electrolyte and glassware, and the observed reproducibility of the results, the second reduction peak is unlikely to be the reduction of impurities. However we can not completely rule out effect of impurities, especially phosphate ions that may be present on the nickel electrode after the electropolishing step. It is known that ppm amounts of iron impurities and other metal impurities can change the shape of the voltammogram especially at slow sweep rates [72].

More than one monolayer is involved in NiOOH peak, for example the charge (1.35 V to 1.5 V) for the fifth cycle corresponds to around 20 monolayers, assuming 257 μC cm^{-2} per monolayer, which means that intercalation of OH^- and anions can have a great influence on the mechanism of the oxidation.

Higher charge (total charge, without the double layer charge correction, 1.35 V to 1.5 V for the oxidation and 1.45 V to 1.25 V for the reduction) for oxidation (Q_{ox}/Q_{red}=1.6 for the 5th cycle) and, the lower admittance ($Y_{peak,ox,52Hz}/Y_{peak,red,52Hz}$=0.79) for this process compared to the reduction can be explained by state of the charge of the nickel electrode. It is possible that in oxidation cycle nickel hydroxide with valence of two oxidizes to valences higher than three (the valence for NiOOH) but in the reduction it does not reduce back to same valence of two. Corrigan had suggested reduction to state charge of 2.5 during the discharge [47]. They proposed the reaction (3.1) to be more accurate than the conventional one electron transfer usually proposed for nickel hydroxide to oxyhydroxide. They balanced this reaction by OH^-, however it can be balanced by H^+, depending on the diffusing species involved in this

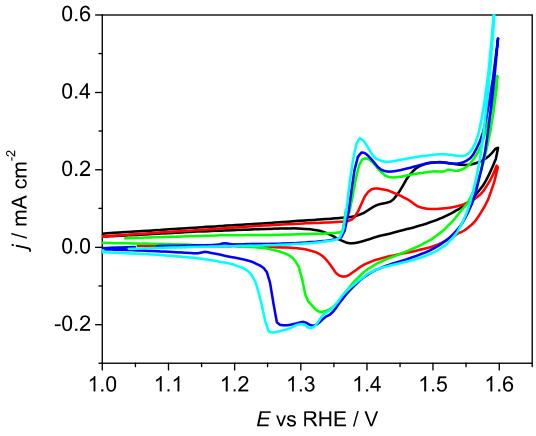

Figure 3.1: NiOOH peak growth by cycling. black:first cycle, red:second cycle, green:5th cycle, blue: 9th cycle, light blue:18th cycle.

transformation process.

$$Ni(OH)_2 + 0.33K^+ + 2OH^- \rightarrow 0.33K(NiO_2)_3 + 2H_2O + 1.67e^- \quad (3.1)$$

A higher rate of reduction as can be seen in the admittance at 3 Hz in Fig. 3.2, is partly related to the lower conductivity of β-$Ni(OH)_2$ [10^{-13}-10^{-15} S m^{-1}] compared to β-NiOOH (10^{-3} S m^{-1}) [8], which is due to the smaller distance between Ni centres in NiOOH compared to $Ni(OH)_2$ that makes charge transfer faster and easier [7]. This is in agreement with galvanostatic discharge experiments where the potential decreased more when $Ni(OH)_2$ was more prevalent on the surface than NiOOH [73]. The higher charge of oxidation compared to reduction implies that the surface does not come back to its initial condition and some NiOOH is accumulated on the surface of $Ni(OH)_2$ in each cycle [47,74]. Also, increase in both reduction and oxidation charge by cycling was observed that shows involvement of multilayers in the $Ni(OH)_2$/NiOOH transformation. Comparing the currents or charges in Fig. 3.1 and admittances, the difference between second and 9th cycle at the potential range of 1.5 V to 1.6 V, is more observable in the CV. This means, at these potentials, enough NiOOH is present

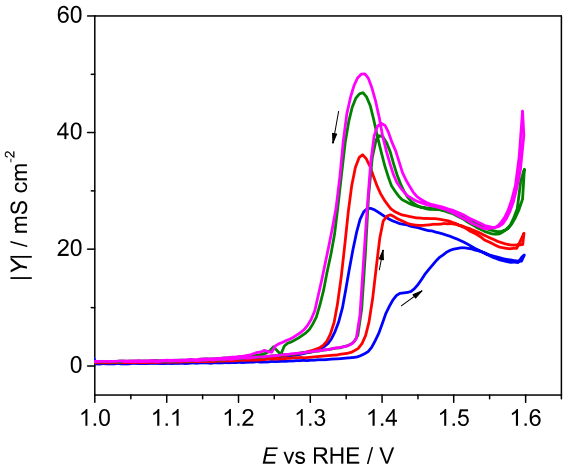

Figure 3.2: Dependence of admittance at 3 Hz on Potential and number of cycles, without glycerol. Blue: first cycle nickel, red:second cycle, green: 9th cycle, magenta:last(18th) cycle.

and the rate is not limited by the conductivity of the $Ni(OH)_2$. The same trend can be seen in Fig. 3.3.

In Fig. 3.4, the capacitance has been calculated using imaginary part of the impedance at 900 Hz. Higher capacitance can be observed in the reduction region, also the change in the surface condition is more drastic in the first cycles.

Different anions have different adsorption energies to the internal layers of the oxide or catalyst surface. The positive charge due to presence of Ni^{3+} and Ni^{2+} is balanced by adsorption of anions. Water adsorption occurs simultaneously to optimize columbic interactions; the presence and adsorption of water may lead to deprotonation which can help to further balance the charge. OH^- adsorption/intercalation is probable because of its higher concentration compared to other anions in alkaline solution, and also the possible hydrogen bonding between OH^- and water in the interlayer spacing. The absorption energy depends on several factors such as the valence of the anion and its size. Higher valent anions like carbonate and sulfate can adsorb more strongly than monovalent anions.

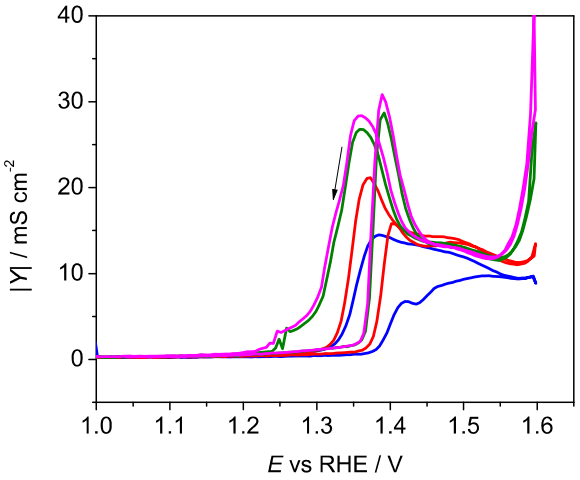

Figure 3.3: Admittance at 1 Hz during NiOOH growth (without glycerol). Blue: first cycle, red:second cycle, green : 9th cycle, magenta:last(18th).

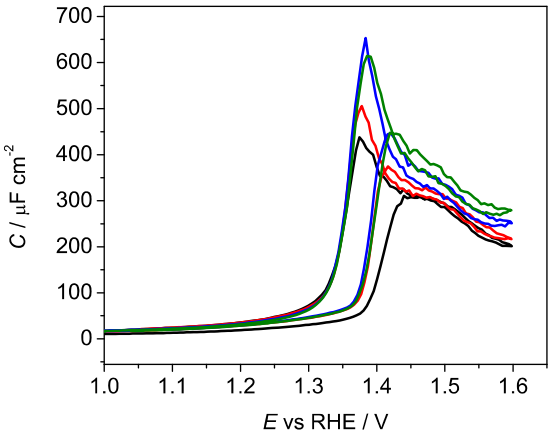

Figure 3.4: Capacitance obtained from imaginary part of impedance at 900 Hz without glycerol. Black: first cycle, red: second cycle, blue: 9th cycle, green: last(18th) cycle.

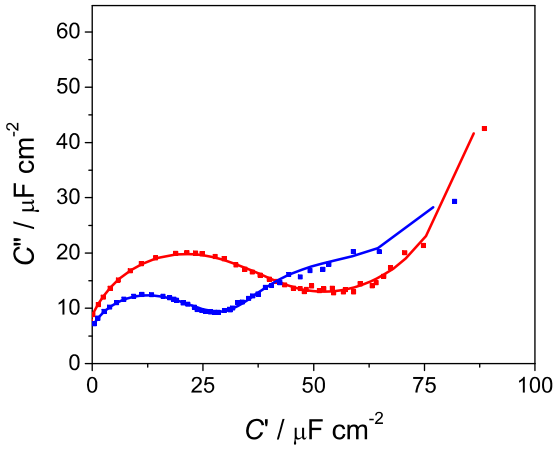

Figure 3.5: Capacitance plot with different features in different number of cycles. Red: Forward second cycle without glycerol fitted with CPE and R_{ct} at 1.297 V, blue: Forward last cycle without glycerol fitted with two CPE and R_{ct} in series at 1.2 V.

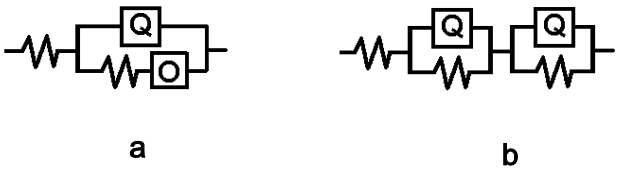

Figure 3.6: Circuits used for fitting the data, a) circuit with finite Warburg, b) at 1.2 V (blue) in Fig. 3.5.

Fig 3.5 shows the fitting results at selected potentials (circuit in Fig. 3.6). In the second cycle near the onset potential the data was fitted with a circuit with one semicircle. In the last cycle at less positive potentials the data shows two semicircles in capacitance plots, and fitting the data with two semicircles gave much better χ^2 compared to one semicircle (F-test can't be used, because more than one element is added to the circuit).

Fig. 3.7 shows the finite Warburg behaviour seen after the peak potential.

In Fig. 3.8, dEIS shows lower polarization resistance compared to slope of voltammogram that indicates presence of slower processes except in the small potential window close to the onset potential, and in the OER region.

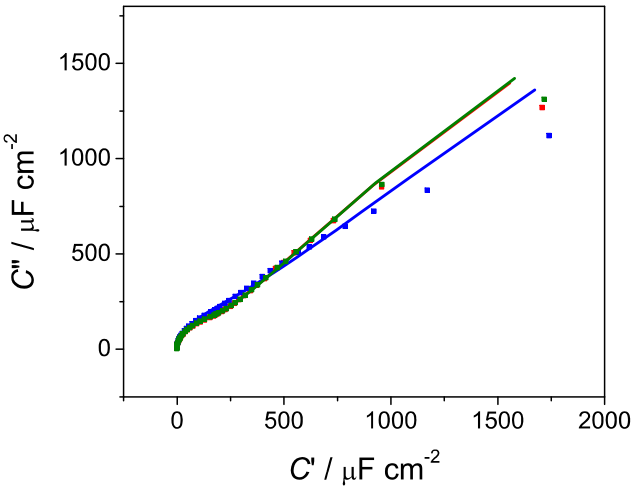

Figure 3.7: Capacitance plot in the potential region where a Warburg element is observed. Red: Forward second cycle without glycerol fitted with Warburg element at 1.506 V, green: second cycle at 1.491 V, blue: Forward last cycle without glycerol fitted with Warburg element at 1.489 V.

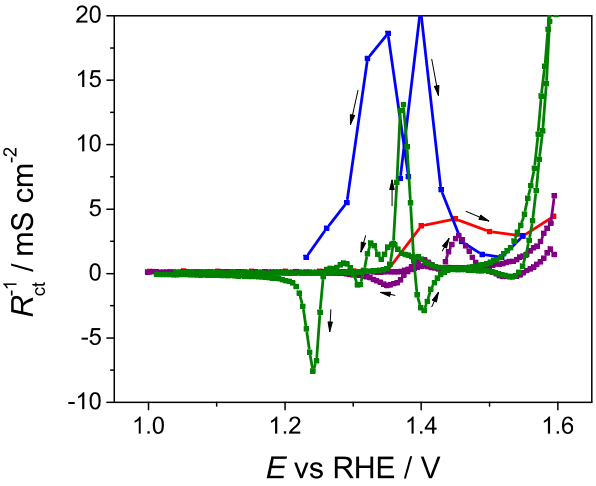

Figure 3.8: Comparison of the slope of CV and R_{ct}^{-1} in the absence of glycerol, obtained by fitting the data with circuit a. Red: R_{ct}^{-1} for first cycle, blue: R_{ct}^{-1} for last cycle, purple: $\frac{\mathrm{d}j}{\mathrm{d}E}$ first cycle, green: $\frac{\mathrm{d}j}{\mathrm{d}E}$ last cycle.

3.1.2 OER

In this section a general summary of oxygen evolution reaction (OER) mechanism is given because NiOOH formation is usually accompanied with OER. Burke et al. [70, 71] proposed the transformation of NiO_x to NiOOH (because of its layered structure) by conditioning to be the reason for the increase in OER activity. The conditioning possibly promotes deposition of iron impurities from alkaline solution (without further purification) to the surface of the nickel electrode.

The Tafel plot from Fig. 3.1 in the OER region (1.55 V to 1.6 V) resulted in a charge transfer coefficient (α) value of 0.78; this value corresponds to a Tafel slope of 75 mV/dec. In the typical approximate analysis, α can be found by adding the number of electrons transferred prior to the RDS (preequilibria reactions) and half the electrons transferred in RDS, where the half is related to the symmetry factor that is usually assumed to be 0.5. This assumption is usually right especially for one electron transfer reactions (RDS is almost always one electron transfer reaction, symmetry factor is related to extent of decrease in activation energy by the increase in the potential). Usually if $\alpha = 0.5$, the first electrochemical reaction can be considered as the RDS. If $\alpha = 1$, a chemical reaction (without electron transfer) is RDS, and is preceeded by a preequilibrium fast electrochemical reaction. The observed reaction can be a combination of these two possible scenarios. The steps for OER and also nickel oxidation consist of formation of bonds between oxygen and nickel in different forms like Ni-O, Ni-O-O, $NiOO^-$, and the RDS is possibly related to nickel oxygen bonding strength [70].

The following mechanism can be considered as part of the set of reactions happening, with modification from Berlinguette [46]. Slope of the voltammograms and R_{ct}^{-1} were close to each other in the OER potential region, it means that one step is RDS. Based on the observed (α) value of 0.78, that possibly corresponds to first electrochemical step as a RDS, we propose reaction (3.2) to be RDS, and the following steps

to be fast reactions. Our suggested mechanism is in agreement with the results of Koper's group [75], where they studied the effect of pH on OER without any purification of solutions and proposed that NiOOH deprotonation and active oxygen species (peroxides and superoxides) formation is rate determining step, and attributed the higher OER activity at higher pH to the promotion of deprotonation at higher pH. So, in the reaction (3.2) NiOOH first deporotonates, then NiOO reacts with either OH^- or H_2O to form oxygen. Also, Bell group suggetsed the formation of OOH(ads) as RDS [76], so there is an agreement in the literature on the peroxide or superoxide nature of the RDS product.

$$NiOOH + OH^- \xrightarrow{\text{slow}} NiOO + H_2O + e^- \tag{3.2}$$

$$NiOO + OH^- \rightarrow NiOH^- + O_2 \tag{3.3}$$

$$NiOO + 2OH^- \rightarrow Ni(OH)_2 + O_2 + 2e^- \tag{3.4}$$

$$NiOO + H_2O \rightarrow Ni(OH)_2 + 0.5O_2 \tag{3.5}$$

$$NiOOH + OH^- \rightarrow NiOH^- + HO_2^- \tag{3.6}$$

$$HO_2^- \rightarrow OH^- + 0.5O_2 \tag{3.7}$$

Chapter 4

Electrooxidation of Glycerol: dEIS Study

In this chapter results for glycerol electrooxidation mechanism are discussed.

4.1 Experimental

The working electrode was nickel wire (0.5 mm diameter, Sigma-Aldrich, 99.9% purity) sealed in heatshrink teflon tubing with about 0.6 cm exposed to the solution. The electrolyte was 0.5 M KOH prepared from semiconductor grade KOH (Sigma Aldrich, 99.99%) and Millipore Milli-Q water. Glycerol (Sigma Aldrich, >99.5%) was added to KOH solution to make 0.1 M glycerol solution. All the experiments were done at 5 mV s^{-1}.

4.2 Results and Discussion

In voltammograms in the presence of glycerol in Fig. 4.1, a decrease in activity by cycling is observed that is possibly due to the decrease in NiOOH formation and

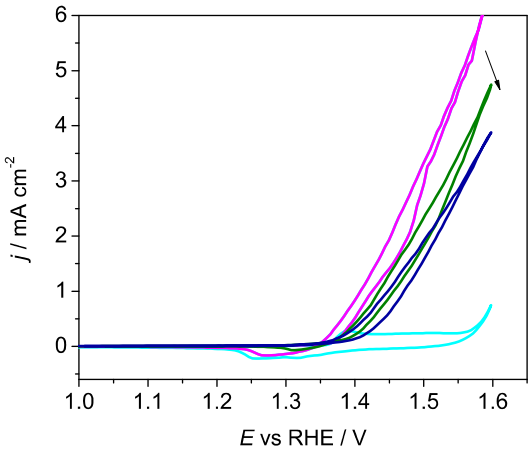

Figure 4.1: CV at 5 mV s^{-1} in the presence and absence of 0.1 M glycerol. Light blue: last cycle before glycerol addition, magenta: first cycle, green: second cycle, dark blue: last cycle.

surface blockage by glycerol. In the presence of glycerol, there is not any specific feature in the potential range of 1.55 to 1.6 V that is related to OER, so the OER is delayed and possibly moved to higher potentials than 1.6 V. This can be explained by the higher adsorption affinity of $Ni(OH)_2$ toward glycerol than OH^-.

The α found from slope by using the relationship between tafel slope and charge transfer coefficient, $b = 2.303\ (RT/\alpha F)$.

$$j = j_0 \exp\left(\frac{\alpha F}{RT}\eta\right) \tag{4.1}$$

Tafel analysis after adding glycerol in the first cycle in the potential range of 1.45 V and 1.6 V (Fig. 4.2), results in α value of 0.26 according to Eq. (4.1), and the Tafel slope of 217 mV / dec, that means possibly the first step is RDS. α value for the last forward cycle is 0.34 while plotting $\ln(1/R_{ct})$ as a function of potential (from impedance data) resulted in α value of 0.1. This difference clearly shows the possibility of the presence of an inductor at the low frequency in the impedance data.

The last cycle before adding glycerol (18th cycle), and the first cycle after adding

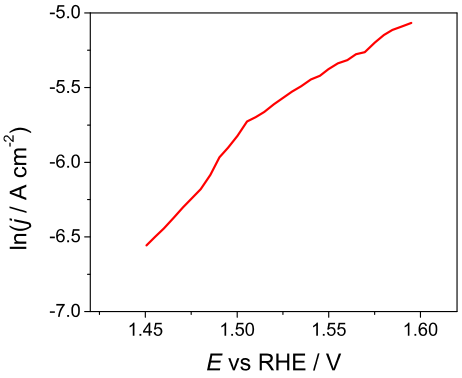

Figure 4.2: Tafel plot for the first cycle in the forward sweep, in the presence of glycerol.

it, have almost the same behaviour in the potential region of 1.35 V and 1.45 V, the onset potential for NiOOH formation. Possibly after formation of several monolayers of NiOOH in this potential range, the surface becomes more active as a sudden increase in current is observed.

As can be seen in Fig. 4.3 before adding glycerol, the admittance for both oxidation and reduction is higher. After adding glycerol in first cycle, initially oxidation admittance follows the trend same as before adding glycerol, but after around 1.45 V increase in admittance for glycerol oxidation is observed. While in the last cycle of NiOOH (without glycerol) it continues decreasing until 1.56 V, and then increases at higher potentials due to the OER.

In the last cycle in the presence of glycerol, no peak for NiOOH formation is observed, which can be attributed to hindrance of NiOOH from glycerol oxidation intermediates accumulating on the surface.

In the forward sweep in the first and second cycles with glycerol, two peak is appeared, that the first peak is possibly due to NiOOH formation, but in the last no peak is observed and it has delayed to more positive potentials. As NiOOH is the active phase and the rate of glycerol oxidation is dependant on the amount of NiOOH, it can be concluded that formation of nickel oxyhydroxide (as it has been hindered

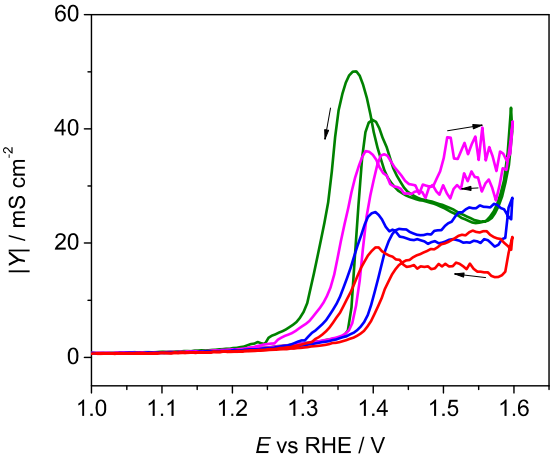

Figure 4.3: Dependence of admittance at 3 Hz on potential and number of cycles in the presence of glycerol. Green: last cycle nickel without glycerol, magenta: first cycle with glycerol, blue: second cycle, and red: last cycle with glycerol.

by glycerol in the last cycle) is the rate limiting step in glycerol oxidation. As can be seen in admittance plot at 3 Hz the admittance of the last cycle without glycerol is almost in the same range as the admittance of the first cycle of glycerol oxidation. Also, after the first cycle in the presence of glycerol the admittance decrease can be associated with a decrease in the amount of NiOOH on the surface, possibly due to the low conductivity of nickel hydroxide or high coverage of oxidation intermediates. As a conclusion after the first cycle lower amount of surface NiOOH and its lower rate of formation (from $Ni(OH)_2$) compared to the glycerol electrooxidation is the limiting step.

Smith et al. [46] observed higher degree of charge trapping in higher thickness nickel hydroxide films using UV spectra and comparing ratio of first anodic charge over cathodic charge, where higher ratio (closer to two) was observed for higher thickness films. Charge trapping means that some part of the surface is stuck in the oxidation state and as a result can not be reduced (more charge for oxidation was observed than for reduction).

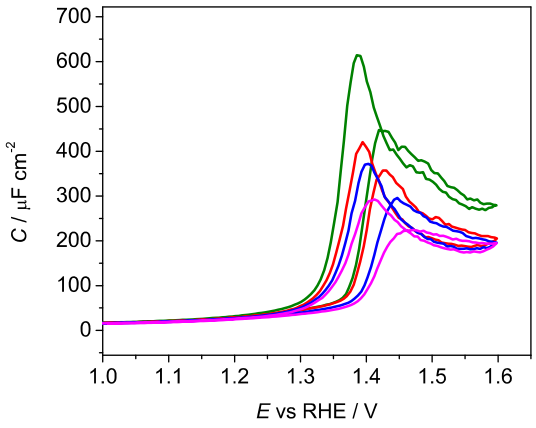

Figure 4.4: Capacitance obtained from the imaginary part of impedance at 900 Hz with glycerol. Green: last cycle without glycerol, red:first with glycerol, blue: second with glycerol, magenta: last(sixth) with glycerol.

Figs. 4.4 shows the capacitance obtained from the imaginary part of the impedance at 900 Hz with glycerol. The peak for oxidation shifts to higher potentials as the number of cycles increases, due to the decreased rate of the NiOOH formation. This decrease in the rate and the need for more potential for NiOOH formation is attributed to the increase in glycerol coverage on the surface and the decrease in the amount of NiOOH on the surface. In the first cycle in the presence of glycerol, because the surface is fully charged (several monolayers of NiOOH is present on the surface) the activity is maximized. In the following cycles, because glycerol oxidation is followed by NiOOH reduction, the amount if NiOOH on the surface has decreased, which will limit the activity for glycerol oxidation.

As can be seen in Figs. 4.5 and 4.6, $\mathrm{d}j/\mathrm{d}E$ and R_{ct}^{-1} are in good agreement in the presence of glycerol. Presence of only one semicircle in the Nyquist plot proves the one step is RDS (possibly two electron transfer oxidation of glycerol to glyceraldehyde) and all other steps are much faster. In the last cycle there is excellent agreement in the forward sweep, but in the backward sweep R_{ct}^{-1} has a lower value than the slope of the CV, which means there are possibly slow relaxation steps in the backward sweep.

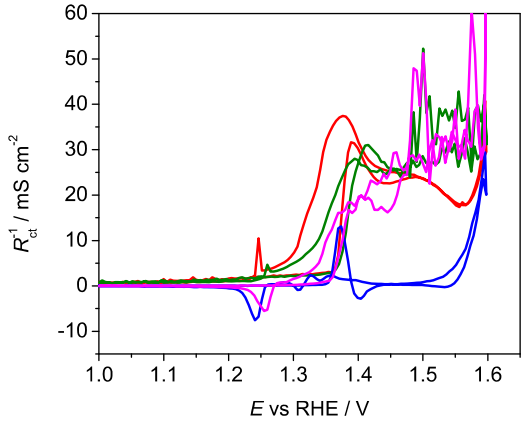

Figure 4.5: Comparison of slope of voltammograms and real part of impedance at 1 Hz. Blue: $\mathrm{d}j/\mathrm{d}E$ last cycle without glycerol, red: R_{ct}^{-1} last cycle without glycerol, magenta: $\mathrm{d}j/\mathrm{d}E$ first with glycerol, green: R_{ct}^{-1} first with glycerol.

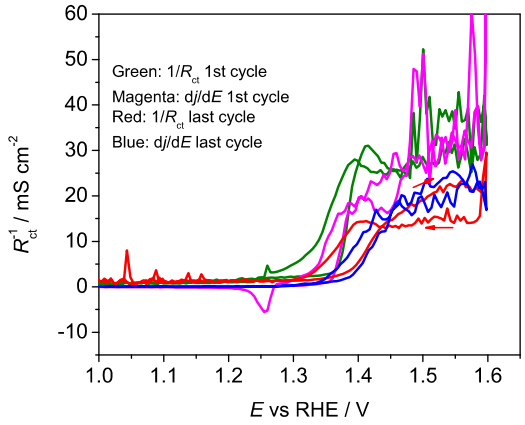

Figure 4.6: Comparison of the slope of the voltammograms and real part of impedance at 1 Hz, all in the presence of glycerol.

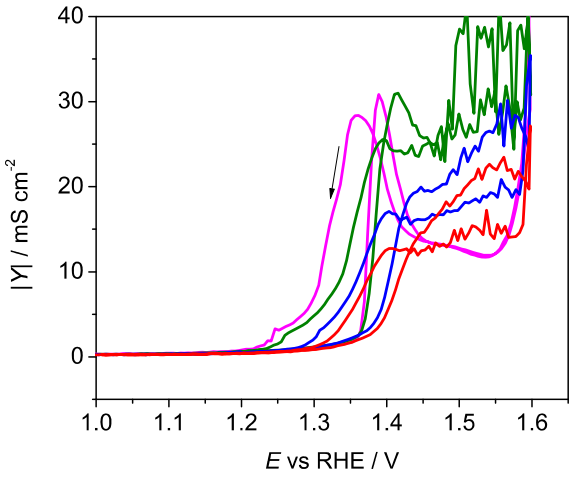

Figure 4.7: Admittance at 1 Hz after glycerol addition. Magenta: before glycerol addition, green: first cycle, blue : second cycle, red: last cycle (6th cycle).

Figure 4.7 shows how the admittance at 1 Hz changes in the presence of glycerol.

Tafel analysis then results in an α value of two, if we assume reaction (1.25) as the preequilibrium step. There is the possibility that reaction (1.25) is not in equilibrium, but is fast in the glycerol oxidation potential region.

Figs. 4.8 and 4.9 shows typical capacitance and Nyquist plots. The capacitance plot shows some scattering in the low frequency region, while the Nyquist plot shows a semicircle. The Nyquist plot shows a higher low frequency intercept in the backward sweep, but as was discussed before, there is the possibility of the presence of an inductor element at lower frequencies that would lead to lowering the polarization resistance and low frequency intercept.

Competitive adsorption of glyceraldehyde decomposition products with OH^- (these products are in their ionic form at this pH, formic acid pK_a: 3.77, glycolic acid: 3.83, glyceric acid: 3.55, Tartronic acid: 2.42, and oxalic acid: 1.25) [17] and possibly higher affinity of the surface toward OH^-, that leads to fast desorption of oxidation products and as a result not further electrochemical oxidation of these products (only chemical decomposition), can be one of the reasons for seeing just one semicircle in

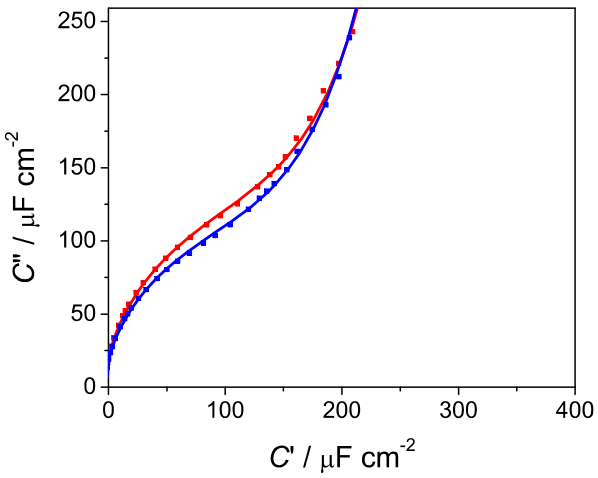

Figure 4.8: Capacitance plot in the presence of glycerol in the first cycle. Red:1.54 V forward sweep, blue:1.54 V backward sweep.

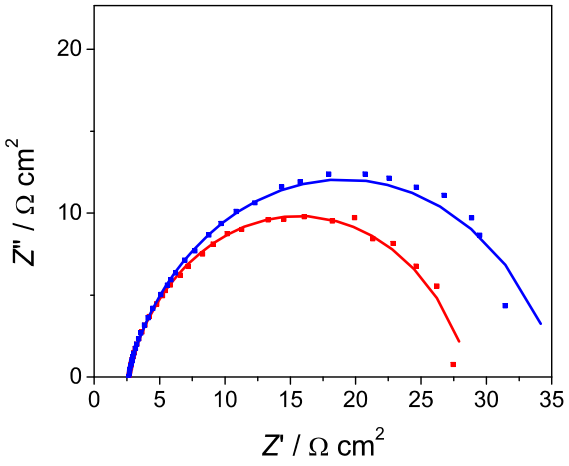

Figure 4.9: Nyquist plot in the presence of glycerol. Red: 1.54 V forward, blue: 1.54 V backward sweep.

the initial stages of glycerol oxidation.

In the absence of glycerol, the impedance of the first forward cycle was fitted with a parallel combination of a resistor (R_{ct}) and a capacitor (C_{dl}) at potentials more negative than 1.47 V. At higher potentials a finite diffusion element was observed. In the backward sweep until 1.4 V, a Randles circuit with a finite Warburg element, with transmittance boundary condition, in series to charge transfer resistance was chosen (circuit a in Fig. 3.6). In the backward sweep at potentials less than 1.4 V, again only charge transfer and double layer charging processes were observed. In the second forward cycle at potentials more positive than 1.42 V, the Warburg element again appeared until potentials around 1.35 V in backward sweep. The last cycle was more complicated: In the forward sweep initially instead of one time constant, a two time constant circuit (circuit b in Fig. 3.6) gave better χ^2 values. Then in the potential range of 1.35 to 1.55 V again one time constant process was used for fitting and extracting the effective capacitance. However diffusion element could be seen (45 degree line in Nyquist plot), two time constant process (circuit b in fig. 3.6) would give a better χ^2 value.

In the presence of glycerol, two time constants were observed until 1.28 V, then just diffusion until 1.38 V. At more positive potentials and in the backward sweep until 1.26 V, charge transfer and double layer charging processes were observed, and then diffusion at less positive potentials until around 1.16 V, and finally two time constant process at less positive potentials.

Fig. 4.10 shows that in the potential range of 1 to 1.3 V, the capacitance increases from about 15 μF cm^{-2} to 40 μF cm^{-2}, and then suddenly increases at more positive potentials. In the NiOOH region (1.3 to 1.6 V), the capacitance increases as the number of cycles increases, in the absence of glycerol and, it decreases in the presence of glycerol, following the same trend as current.

Figures 4.12-4.15 show the results of fitting to equivalent circuits (Randles circuit).

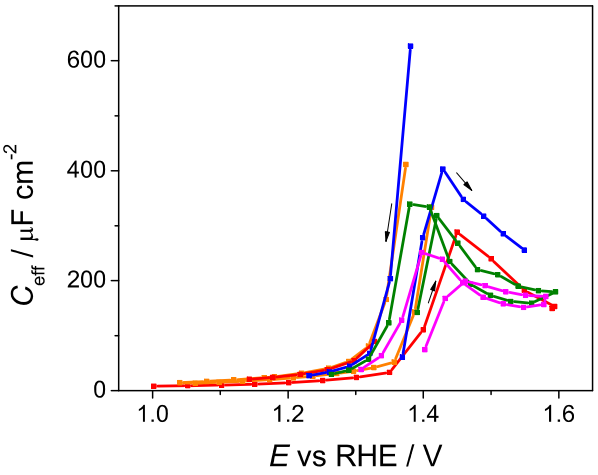

Figure 4.10: Effective capacitance calculated using Brug equation. Red: first cycle without glycerol, orange: second cycle without glycerol, blue: last cycle without glycerol, green: first cycle with glycerol, magenta: last cycle with glycerol

In the presence of glycerol in the first cycle, warburg element was observed in the potential region of 1.3 to 1.36 V, CPE increased from 1.13×10^{-4} to 2.18×10^{-4} S s^{n} cm^{-2}, n decreased from 0.87 to 0.84, and R increased from 198 Ω cm^2 at 1.3 V to 276 Ω cm^2 at 1.33 V and 283 Ω cm^2 at 1.36 V. Admittance of Warburg element (Eq. 4.2) increased from 3.27×10^{-4} to 5.44×10^{-4} to 0.0016 S cm^{-2} in this potential range, also b element decreased from 0.8505 to 0.6734 and to 0.5379 s$^{0.5}$. Eq. 4.2 is a general form of a Warburg element with transmittance boundary conditions, where b and Y_{warb} depend on diffusion coefficients, thickness of the diffuse layer, concentrations of adsorbed species and reaction rates.

$$Y = Y_{\mathrm{warb}}\sqrt{\mathrm{i}\omega}\ \coth(b\sqrt{\mathrm{i}\omega}) \tag{4.2}$$

For a simpler case of a finite Warburg element with transmittance boundary condition for a single species reversible diffusion, the parameters can be written as [77] :

$$Y_{\text{warb}} = \frac{z^2 F^2 \sqrt{D} C^*}{RT} \tag{4.3}$$

$$b = \frac{d}{\sqrt{D}} \tag{4.4}$$

where d is the thickness of diffusion layer, and z can be assumed to be one in the present case.

The above mentioned admittances for the Warburg element result in $C^*\sqrt{D}$=8.65×10^{-11}, 10^{-10}, 4×10^{-10} mol m^{-2} s$^{-0.5}$, at 1.3 V, 1.33 V, and 1.36 V, respectively.

Assuming the diffusion coefficient of 10^{-9} m^2 s^{-1}, results in C^* in the range of 3×10^{-9} mol L^{-1}, it can be either H^+ or OH^-, and d in the range of 30 μm, which agrees with the film thickness (electrode with the diameter of 500 μm was used for the experiments).

Fig. 4.11 shows the voltammogram slopes and R_{ct}^{-1}, in the presence of glycerol. It is interesting to note that charge transfer and current trends are opposite in the forward and backward sweep. The backward sweep has higher current than the forward sweep, while dEIS shows higher charge transfer resistance in the backward sweep. The reason is the slower process that leads to lower R_{p} (inductor in the equivalent circuit), which is possibly because of oxidation of the rest of the adsorbed species by some kind of reactivation of the surface in the backward sweep. The slopes and currents in the forward and backward sweeps are close to each other, which shows the fast nature of glycerol oxidation.

Fig. 4.12 shows that in the potential range where the Warburg element was observed in the impedance data, the Y_{CPE} decreases going to more positive potentials, that possibly shows double layer discharging. These values are slightly high for the double layer capacitance that may be related to presence of another time constant in addition to double layer charging. Also, the actual capacitance is lower than the

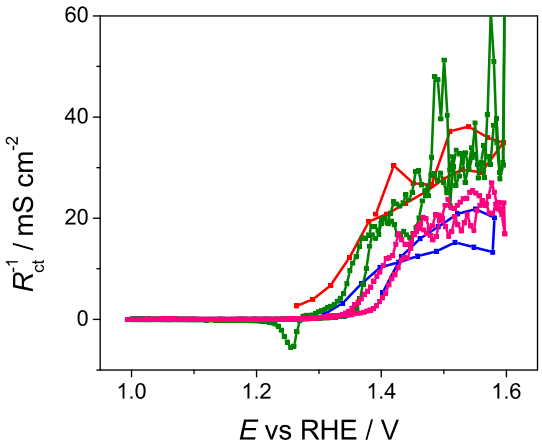

Figure 4.11: Comparison of the slope of voltammogram and R_{ct}^{-1} in the presence of glycerol, 5 mV s^{-1}. Red: R_{ct}^{-1} for first cycle, blue: R_{ct}^{-1} for last cycle, green: $\frac{\mathrm{d}j}{\mathrm{d}E}$ first cycle, pink: $\frac{\mathrm{d}j}{\mathrm{d}E}$ last cycle.

admittance of the CPE, for example fitting the data at 1.55 V in the second cycle, with a capacitor instead of CPE resulted in 160 μF cm^{-2}, however Y_{CPE} is around 500 μS s$^{\mathrm{n}}$ cm^{-2}.

The exponent for the CPE is higher at more positive potentials, indicating a more ideal double layer capacitor.

Fig. 4.14 shows that the first cycle has higher resistance than the last cycle, which makes sense. In the absence of glycerol and at higher potential, the charge transfer resistance is lower and Warburg element is present, which means diffusion must have an influence. This shows that possibly diffusion is the rate limiting process.

A decrease in the Warburg parameter is observed in the absence of glycerol in Fig. 4.15 on going to more positive potentials, which means a decrease in $c^{*}\sqrt{D}$. This three times decrease from 15 to around 5 mS cm^{-2} is possibly related to a change in concentration, and not to the diffusion coefficient.

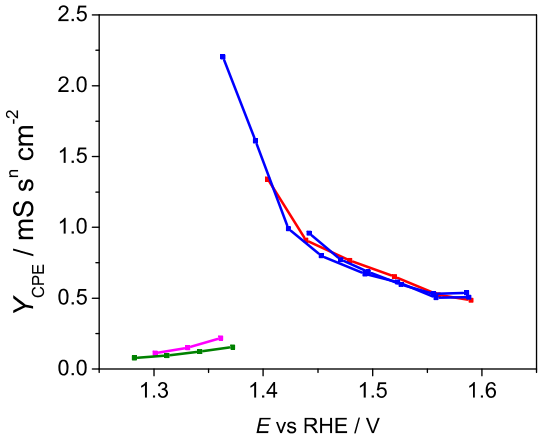

Figure 4.12: CPE parameter of Warburg circuit. Red: first cycle without glycerol backward sweep , blue: second cycle without glycerol, pink: first cycle and green: second cycle backward sweep in the presence of glycerol.

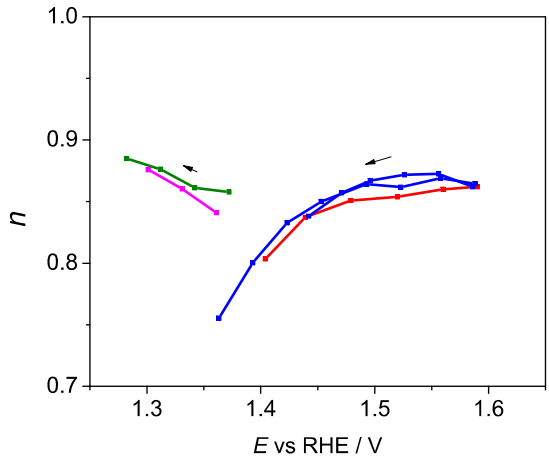

Figure 4.13: CPE exponent(n) of Warburg circuit. Red: first cycle without glycerol backward sweep , blue: second cycle without glycerol, pink: first cycle and green: second cycle backward sweep in the presence of glycerol.

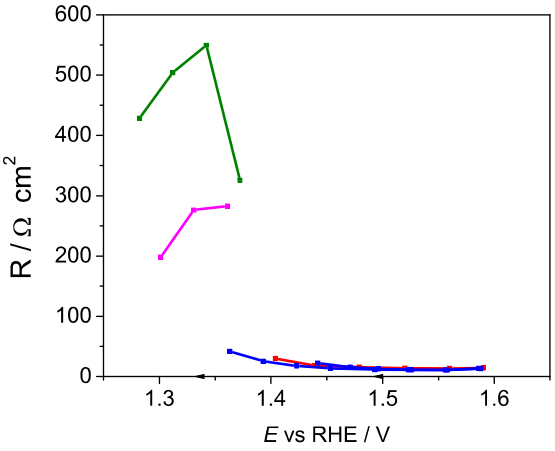

Figure 4.14: Resistance values in the Warburg circuit (Randles). Red: first cycle without glycerol backward sweep , blue: second cycle, pink and green: backward sweep in the presence of glycerol, first and last cycle, respectively.

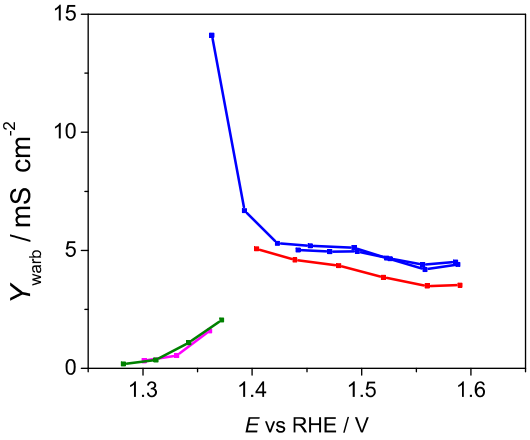

Figure 4.15: Finite Warburg parameter (Y_{warb}). Red: first cycle without glycerol backward sweep , blue: second cycle, pink and green: backward sweep in the presence of glycerol, first and last cycle, respectively.

4.2.1 Glycerol oxidation mechanism

As discussed in the first chapter, either reaction (1.23) or (1.24) is in the catalytic cycle with reaction (1.25), where NiOOH reduction to $Ni(OH)_2$ provides the electrons for the oxidation of glycerol. In dEIS experiment in the presence of glycerol, one semicircle was observed, also voltammograms had the same slope as R_{ct}^{-1} proving that one step is RDS. Observed charge transfer coefficient of 0.25 can be interpreted as the first electrochemical step to be RDS. So the, reaction (1.23) is more likely to be rate limiting step, the alternative proposed mechanism is reactions, (1.19), (1.20) and (1.25) to be in catalytic cycle, and reaction (1.19) as RDS. This is a electrochemical reaction where simultaneous oxidation to glyceraldehyde, and reduction to $Ni(OH)_2$ occurs. These results are in agreement with the literature data [51, 53, 54], where using HPLC, formation of glyceraldehyde was proposed to be the rate limiting step, and further oxidation of glyceraldehyde to other products a fast reaction.

Chapter 5

Conclusions and Further Work

5.1 Conclusions and Contributions

Nickel has a great potential to replace precious metals like platinum. Understanding the mechanism of the formation of the $Ni(OH)_2$ that is a precursor for formation of NiOOH, that is the active phase for OER, opens new windows for the development of more active materials. There are so many occasions in the literature where they fail to answer whether the activity of the electrocatalyst is related to the surface area or the intrinsic activity, this thesis tried to answer to questions on how different phase of nickel oxide are converting in to each other and what is the intrinsic activity of the nickel for glycerol oxidation. Finding out the mechanism for this interconversion helps to have better control on the amount of the active phase on the surface of the electrocatalyst.

Glycerol when completely oxidized, provides high density energy. Answering the question on mechanism of glycerol oxidation helps to understand whether there are valuable intermediate products involved in this process. Analytical tools have been previously used to qunatify the electrooxidation products and propose a mechanism for this process [51,53,54]. Different mechanisms and different products were observed

at different pH. It is well agreed in the literature that glyceraldehyde formation is the pathway for electrooxidation in alkaline solution, and glyceraldehyde decomposes in the alkaline solution.

In this study dynamic changes of the surface condition of the nickel electrode were studied by dEIS, which provided information about the potential dependent double layer capacitance and charge transfer resistance. dEIS was found to be a better tool for studying alcohol oxidation, where the reaction was faster. dEIS is a strong complementary technique to analytical techniques like HPLC, that provides information on rate limiting steps and number of steps that are invloved in RDS.

A decrease in the capacitance due to formation of hydrogen bonding in the inter-layer spacing of α-$Ni(OH)_2$ was observed in the early stages of nickel oxidation. A Warburg element, attributed to proton or OH^- diffusion was observed in the NiOOH potential region. dEIS for glycerol electrooxidation showed one semicircle and analysis of the data suggested the presence of an inductor at lower frequencies and it was concluded that the reaction proceeds via formation of glyceraldehyde that chemically converts to other products.

5.2 Future Work

The following items can be suggested for further studies:

1) Mathematical modelings for different mechanisms can be solved and compared to experimental results to verify the proposed mechanism.

2) A microfluidic cell can be used to extend the application and study adsorbed species on the surface by coupling with Raman and FTIR. It can help to see the intermediate species on the surface and propose a better mechanism that supports formation of those species.

3) Different product quantification methods such as HPLC or mass spectroscopy

can be used in situ to study product distribution in real time for glycerol oxidation. Finding the intermediate species using in situ analytical measurements helps to better understand further oxidation of glyceraldehyde and the half life of the intermediate species.

4) pH and concentration effects are the most important factors that should be studied. Preliminary experiments have shown that there is an optimum concentration where the highest current can be achieved, higher concentrations than this optimum value probably lead to surface deactivation due to surface blockage by adsorbed glycerol. The effect of pH and proton or hydroxide diffusion on nickel hydroxide and oxyhydroxide formation will provide more information on the mechanism and how the mechanism changes in different environments. In this study diffusion of protons were observed during NiOOH formation, further pH experiments helps to see if there is any competitive contribution of the hydroxide and protons in the mechanism.

5) The effect of iron impurities on the OER has been studied in the literature. It would be interesting to study the effect of iron on glycerol oxidation. Bimetallic catalysts such as Ni/Fe , Ni/CeO_2, and nickel as a component in MOF, would be studied to reduce the overpotential and enhance the rate of glycerol oxidation.

6) The experimental setup can be improved by separating the working and counter electrode compartments, with an ion exchange membrane. This can help avoiding oxygen produced at the counter electrode affecting the working electrode. A Schlenk line setup would also be used to avoid the oxgygen and carbon dioxide from the open atmosphere to dissolve into the solution. This helps to have more realistic viewpoints on the activity of nickel on oxygen reduction reaction.

7) dEIS can be coupled with EQCM and XPS to get further insight on adsorbed species and mechanism. In situ potential hold experiments in the ambient pressure XPS setup will help to answer the remaining questions about the mechanism. In a pioneering research Hecht [78] used impedance and XPS to study Ag oxidation in

the presence of NaCl in HCl or NaOH solutions, and observed lower Cl^- and higher Na^+surface concentrations in alkaline solution. This was explained by replacing the chloride ion by hydroxide ion in the inner Holmholtz layer in alkaline solution. Also, underpotential deposition of oxide layer was observed in alkaline solution that resulted in more decrease in Cl^- adsorption. Also a plot of sum of concentrations (c_{Na^+} - c_{Cl^-} - c_{OH^-}) as a function of potential showed a linear line with the same negative slope in both alkaline and acidic solutions. So this combination opens a new avenue for getting more details about the complete mechanism.

8) The temperature dependence of nickel oxide species formation and glycerol oxidation can be studied to find the activation energies. It is interesting to know the difference between the activation energy of α-$Ni(OH)_2$ to γ-NiOOH and β-$Ni(OH)_2$ to β-NiOOH conversions.

9) Comparing the results by purging with argon, hydrogen and oxygen can give more insight about the mechanism of HER and hydrogen oxidation reaction.

10) Improving the setup and designing the experiments to find the answer to the following questions can be valuable: What are the nature of the slow processes occuring? Why does the slope of CV not match the inverse of the polarization resistance? Would they match after considering the slower processes (using lower frequencies)?

11) Potential is found to be an important factor for oxidation of nickel. Adding alternative oxidants like hydrogen peroxide into the solution may give further information about the mechanism.

References

[1] E. Barsoukov and J. R. Macdonald, *Impedance Spectroscopy: Theory, Experiment, and Applications*, John Wiley & Sons, 2018.

[2] G. S. Popkirov and R. N. Schindler, *Electrochimica Acta*, 1995, **40**(15), 2511–2517.

[3] G. S. Popkirov, *Electrochimica Acta*, 1996, **41**(7-8), 1023–1027.

[4] D. A. Harrington, *Journal of Electroanalytical Chemistry*, 1993, **355**(1-2), 21–35.

[5] A. J. Tkalych, K. Yu, and E. A. Carter, *The Journal of Physical Chemistry C*, 2015, **119**(43), 24315–24322.

[6] F. Dionigi and P. Strasser, *Advanced Energy Materials*, 2016, **6**(23), 1600621.

[7] P. Oliva, J. Leonardi, J. F. Laurent, C. Delmas, J. J. Braconnier, M. Figlarz, F. Fievet, and A. de Guibert, *Journal of Power Sources*, 1982, **8**, 229–255.

[8] J.-L. Bantignies, S. Deabate, A. Righi, S. Rols, P. Hermet, J.-L. Sauvajol, and F. Henn, *The Journal of Physical Chemistry C*, 2008, **112**(6), 2193–2201.

[9] K. I. Pandya, R. W. Hoffman, J. McBreen, and W. E. O'Grady, *Journal of The Electrochemical Society*, 1990, **137**(2), 383–388.

[10] M. D. Symes, Y. Surendranath, D. A. Lutterman, and D. G. Nocera, *Journal of the American Chemical Society*, 2011, **133**(14), 5174–5177.

[11] K. Sun, N. Park, Z. Sun, J. Zhou, J. Wang, X. Pang, S. Shen, S. Y. Noh, Y. Jing, S. Jin, P. K. L. Yu, and D. Wang, *Energy and Environmental Science*, 2012, **5**(7), 7872–7877.

[12] X. Wang, H. Luo, H. Yang, P. J. Sebastian, and S. A. Gamboa, *International Journal of Hydrogen Energy*, 2004, **29**(9), 967–972.

[13] A. Singh, M. Fekete, T. Gengenbach, A. N. Simonov, R. K. Hocking, S. L. Y. Chang, M. Rothmann, S. Powar, D. Fu, Z. Hu, Q. Wu, Y.-B. Cheng, U. Bach, and L. Spiccia, *ChemSusChem*, 2015, **8**(24), 4266–4274.

[14] G. C. Sedenho, P. T. Lee, H. S. Toh, C. Salter, C. Johnston, N. R. Stradiotto, and R. G. Compton, *The Journal of Physical Chemistry C*, 2015, **119**(12), 6896–6905.

[15] S.-J. Li, W. Guo, R.-T. Liu, and J.-M. Du, *International Journal of Electrochemical Science*, 2016, **11**, 7604–7690.

[16] N. R. Stradiotto, K. E. Toghill, L. Xiao, A. Moshar, and R. G. Compton, *Electroanalysis*, 2009, **21**(24), 2627–2633.

[17] V. L. Oliveira, C. Morais, K. Servat, T. W. Napporn, G. Tremiliosi-Filho, and K. B. Kokoh, *Journal of Electroanalytical Chemistry*, 2013, **703**, 56–62.

[18] J. M. Falkowski, N. M. Concannon, B. Yan, and Y. Surendranath, *Journal of the American Chemical Society*, 2015, **137**(25), 7978–7981.

[19] E. M. Miner, T. Fukushima, D. Sheberla, L. Sun, Y. Surendranath, and M. Dinca, *Nature communications*, 2016, **7**, 10942–10948.

[20] H. Bode, K. Dehmelt, and J. Witte, *Electrochimica Acta*, 1966, **11**(8), 1079–1088.

[21] B. MacDougall and M. Cohen, *Journal of The Electrochemical Society*, 1974, **121**(9), 1152–1159.

[22] F. Hahn, D. Floner, B. Beden, and C. Lamy, *Electrochimica acta*, 1987, **32**(11), 1631–1636.

[23] A. Seyeux, V. Maurice, L. H. Klein, and P. Marcus, *Journal of Solid State Electrochemistry*, 2005, **9**(5), 337–346.

[24] R. N. O'Brien and K. V. N. Rao, *Journal of The Electrochemical Society*, 1965, **112**(12), 1245–1248.

[25] A. K. M. S. Huq and A. J. Rosenberg, *Journal of The Electrochemical Society*, 1964, **111**(3), 270–278.

[26] H.-W. Hoppe and H.-H. Strehblow, *Corrosion Science*, 1990, **31**, 167–177.

[27] L. Zhang and D. D. Macdonald, *Electrochimica acta*, 1998, **43**(18), 2673–2685.

[28] F. T. Wagner and T. E. Moylan, *Journal of The Electrochemical Society*, 1989, **136**(9), 2498–2506.

[29] R. E. Hummel, R. J. Smith, and E. D. Verink Jr, *Corrosion Science*, 1987, **27**(8), 803–813.

[30] W.-K. Paik and Z. Szklarska-Smialowska, *Surface Science*, 1980, **96**(1-3), 401–412.

[31] T. Okazawa, T. Nishizawa, T. Nishimura, and Y. Kido, *Physical Review B*, 2007, **75**(3), 33413.

[32] C.-C. Hu and T.-C. Wen, *Electrochimica Acta*, 1998, **43**(12-13), 1747–1756.

[33] D. S. Hall, C. Bock, and B. R. MacDougall, *ECS Transactions*, 2013, **50**(31), 165–179.

[34] M. A. Reid and P. L. Loyselle, *Journal of Power Sources*, 1991, **36**(3), 285–298.

[35] X. Shi, D. E. Simpson, M. J. Walters, C. M. Pettit, and D. Roy, *Journal of The Electrochemical Society*, 2014, **161**(9), H583—-H592.

[36] J. Katić, M. Metikoš-Huković, R. Peter, and M. Petravić, *Journal of Power Sources*, 2015, **282**, 421–428.

[37] J. Katić, M. Metikoš-Huković, and I. Milošev, *Journal of The Electrochemical Society*, 2015, **162**(14), C767–C774.

[38] F. Seland, R. Tunold, and D. A. Harrington, *Electrochimica Acta*, 2006, **51**(18), 3827–3840.

[39] H.-W. Hoppe and H.-H. Strehblow, *Surface and Interface Analysis*, 1989, **14**(3), 121–131.

[40] R. Barnard and C. F. Randell, *Journal of Applied Electrochemistry*, 1983, **13**(1), 27–38.

[41] R. L. Doyle, I. J. Godwin, M. P. Brandon, and M. E. G. Lyons, *Physical Chemistry Chemical Physics*, 2013, **15**(33), 13737–13783.

[42] S. Klaus, Y. Cai, M. W. Louie, L. Trotochaud, and A. T. Bell, *The Journal of Physical Chemistry C*, 2015, **119**(13), 7243–7254.

[43] T. Takasaki, K. Nishimura, T. Mukai, T. Iwaki, K. Tsutsumi, and T. Sakai, *Journal of The Electrochemical Society*, 2012, **159**(11), A1891—-A1896.

[44] D. M. MacArthur, *Journal of The Electrochemical Society*, 1970, **117**(4), 422–426.

[45] D. M. MacArthur, *Journal of The Electrochemical Society*, 1970, **117**(6), 729–733.

[46] R. D. L. Smith, R. S. Sherbo, K. E. Dettelbach, and C. P. Berlinguette, aug , 2016, **28**(16), 5635–5642.

[47] D. A. Corrigan, *Journal of The Electrochemical Society*, 1989, **136**(3), 613.

[48] M. Pagliaro, R. Ciriminna, H. Kimura, M. Rossi, and C. Della Pina, *Angewandte Chemie*, 2007, **119**(24), 4516–4522.

[49] C.-H. C. Zhou, J. N. Beltramini, Y.-X. Fan, and G. Q. M. Lu, *Chemical Society Reviews*, 2008, **37**(3), 527–549.

[50] O. M. Daniel, A. DeLaRiva, E. L. Kunkes, A. K. Datye, J. A. Dumesic, and R. J. Davis, *ChemCatChem*, 2010, **2**(9), 1107–1114.

[51] Y. Kwon, K. J. P. Schouten, and M. T. M. Koper, *ChemCatChem*, 2011, **3**(7), 1176–1185.

[52] R. M. A. Tehrani and S. Ab Ghani, *Electrochimica Acta*, 2012, **70**, 153–157.

[53] M. C. Oliveira V.L. and G. Tremiliosi-Filho, *Electrocatalysis*, 2015, **6**, 447–454.

[54] Y. Kwon, S. C. S. Lai, P. Rodriguez, and M. T. M. Koper, *Journal of the American Chemical Society*, 2011, **133**(18), 6914–6917.

[55] M. Alsabet, M. Grden, and G. Jerkiewicz, *Electrocatalysis*, 2011, **2**(4), 317–330.

[56] B. Beden, D. Floner, J. M. Leger, and C. Lamy, *Surface Science*, 1985, **162**(1-3), 822–829.

[57] D. S. Hall, C. Bock, and B. R. MacDougall, *Journal of The Electrochemical Society*, 2014, **161**(12), H787—-H795.

[58] A. Seyeux, V. Maurice, L. H. Klein, and P. Marcus, *Journal of The Electrochemical Society*, 2006, **153**(11), B453—-B463.

[59] A. Lasia and A. Rami, *Journal of Electroanalytical Chemistry and Interfacial Electrochemistry*, 1990, **294**(1-2), 123–141.

[60] R. Simpraga and B. E. Conway, *Journal of Electroanalytical Chemistry and Interfacial Electrochemistry*, 1990, **280**(2), 341–357.

[61] M. Bernardini, N. Comisso, G. Davolio, and G. Mengoli, *Journal of Electroanalytical Chemistry*, 1998, **442**(1-2), 125–135.

[62] M. Grdeń and K. Klimek, *Journal of Electroanalytical Chemistry*, 2005, **581**(1), 122–131.

[63] A. G. Oshchepkov, A. Bonnefont, V. A. Saveleva, V. Papaefthimiou, S. Zafeiratos, S. N. Pronkin, V. N. Parmon, and E. R. Savinova, *Topics in Catalysis*, 2016, **59**(15-16), 1319–1331.

[64] B. Hirschorn, M. E. Orazem, B. Tribollet, V. Vivier, I. Frateur, and M. Musiani, *Electrochimica Acta*, 2010, **55**(21), 6218–6227.

[65] L. J. Oblonsky and T. M. Devine, *Journal of the Electrochemical Society*, 1995, **142**(11), 3677–3682.

[66] Z. Liang, H. S. Ahn, and A. J. Bard, *Journal of the American Chemical Society*, 2017, **139**(13), 4854–4858.

[67] J. L. Weininger and M. W. Breiter, *Journal of The Electrochemical Society*, 1964, **111**(6), 707–712.

[68] A. Seyeux, V. Maurice, L. H. Klein, and P. Marcus, *Electrochimica Acta*, 2008, **54**(2), 540–544.

[69] L. A. De Faria, M. Prestat, J.-F. Koenig, P. Chartier, and S. Trasatti, *Electrochimica Acta*, 1998, **44**(8-9), 1481–1489.

[70] M. S. Burke, L. J. Enman, A. S. Batchellor, S. Zou, and S. W. Boettcher, *Chemistry of Materials*, 2015, **27**(22), 7549–7558.

[71] M. S. Burke, S. Zou, L. J. Enman, J. E. Kellon, C. A. Gabor, E. Pledger, and S. W. Boettcher, *The Journal of Physical Chemistry Letters*, 2015, **6**(18), 3737–3742.

[72] L. Trotochaud, S. L. Young, J. K. Ranney, and S. W. Boettcher, *Journal of the American Chemical Society*, 2014, **136**(18), 6744–6753.

[73] S. Deabate and F. Henn, may , 2005, **50**(14), 2823–2835.

[74] A. S. Batchellor and S. W. Boettcher, *{ACS} Catalysis*, 2015, **5**(11), 6680–6689.

[75] B. J. Trzesniewski, O. Diaz-Morales, D. A. Vermaas, A. Longo, W. Bras, M. T. M. Koper, and W. A. Smith, *Journal of the American Chemical Society*, 2015, **137**(48), 15112–15121.

[76] D. Friebel, M. W. Louie, M. Bajdich, K. E. Sanwald, Y. Cai, A. M. Wise, M.-J. Cheng, D. Sokaras, T.-C. Weng, R. Alonso-Mori, and Others, *Journal of the American Chemical Society*, 2015, **137**(3), 1305–1313.

[77] V. F. Lvovich, *Impedance spectroscopy: applications to electrochemical and dielectric phenomena*, John Wiley & Sons, 2012.

[78] D. Hecht and H.-H. Strehblow, *Journal of Electroanalytical Chemistry*, 1997, **440**(1-2), 211–217.